Scientific Research Publishing

American Journal of Computational Mathematics, 2025, 15(1), 16-57
https://www.scirp.org/journal/ajcm
ISSN Online: 2161-1211
ISSN Print: 2161-1203

Random Oscillatory and Pulsatory Models in Elliptic Functions

Victor A. Miroshnikov

Department of Mathematics and Data Analytics, School of Natural and Mathematical Sciences, University of Mount Saint Vincent, New York, USA
Email: victor.miroshnikov@umsv.edu

How to cite this paper: Miroshnikov, V.A. (2025) Random Oscillatory and Pulsatory Models in Elliptic Functions. *American Journal of Computational Mathematics*, **15**, 16-57.
https://doi.org/10.4236/ajcm.2025.151002

Received: December 30, 2024
Accepted: February 10, 2025
Published: February 13, 2025

Abstract

To explore experimental quantization of stochastic chaos and exact wave turbulence in exponential oscillons, it is necessary to construct smooth random functions of time. In the current paper, we develop a new method of modeling stochastic variables described by a closed system of ordinary differential and algebraic equations. Primarily, oscillatory and pulsatory dynamic models produced by the first triplet of copolar elliptic functions are studied from the viewpoint of the Hamiltonian and Newtonian dynamics. Secondly, the Hamiltonian systems of the first triplet and the first triplet squared are meticulously investigated in the hyperbolic limit that results in oscillations and pulsations with rectangular and point pulses and a variable period. Thirdly, the relative Hamiltonian systems are used to develop two stochastic models of a random oscillatory cn-noise and a random pulsatory cn^2-noise. Numerical experiments show that for the Bernoulli frequencies the random oscillatory cn-noise approaches a smooth random oscillatory variable with an unbounded period and the Gaussian probability distribution and the random pulsatory cn^2-noise tends to a smooth random pulsatory variable with an unbounded period and the truncated Gaussian probability distribution as the number of elliptic modes approaches infinity.

Keywords

Stochastic Chaos, Exact Wave Turbulence, Experimental Quantization, Smooth Random Functions, Truncated Gaussian Probability Distribution

1. Introduction

Experimental implementation of theoretical quantization of stochastic chaos [1] and exact wave turbulence [2] [3] in exponential oscillons and pulsons requires

construction of smooth random functions of time, which will give an opportunity to visualize and analyze experimental quantization, like it was done for deterministic chaos with the Fourier [4] and Bernoulli [5] sets of wave parameters.

Primarily, stochastic variables have been developed with the help of elliptic functions in [6] [7] to model spatiotemporal cascades of exposed, hidden, and dual perturbations of the Couette and Poiseuille-Hagen flows. The cascade approach results in an open-ended system of algebraic equations, where deterministic variables of basic flows are interconnected with random variables of fluid-dynamic perturbations modeling transition and intermittency.

In the current paper, we develop a novel approach to modeling stochastic variables described by a closed system of ordinary differential and algebraic equations, which are separated from deterministic variables of basic flows. The contents of this paper are as follows. In Section 2, oscillatory and pulsatory dynamic models produced by the first triplet of copolar elliptic functions are studied from the viewpoint of the Hamiltonian and Newtonian dynamics. We continue exploration of the first triplet squared in Section 3 using the hyperbolic limit that results in oscillations and pulsations with rectangular and point pulses and a variable period.

Appropriate Hamiltonian systems are used to construct two stochastic models of the random oscillatory cn-noise and the random pulsatory cn^2-noise in Sections 4 and 5, respectively. Numerical experiments show that for the Bernoulli frequencies the random oscillatory cn-noise approaches a smooth random oscillatory variable with an unbounded period and the Gaussian probability distribution and the random pulsatory cn^2-noise tends to a smooth random pulsatory variable with an unbounded period and the truncated Gaussian probability distribution as the number of elliptic modes approaches infinity. Section 6 contains a summary of results on the Hamiltonian systems and the stochastic models.

2. Oscillatory and Pulsatory Dynamic Models of the First Triplet

2.1. Definitions of Elliptic Functions of the First Triplet

Define $[f,g,h](\tau,\varepsilon)$ as the first triplet of copolar elliptic functions $[\mathrm{sn}(\tau,\varepsilon),\mathrm{cn}(\tau,\varepsilon),\ \mathrm{dn}(\tau,\varepsilon)]$, which are called elliptic sine, elliptic cosine, and elliptic dine [8], respectively,

$$f(\tau,\varepsilon)=\mathrm{sn}(\tau,\varepsilon),\ \ g(\tau,\varepsilon)=\mathrm{cn}(\tau,\varepsilon),\ h(\tau,\varepsilon)=\mathrm{dn}(\tau,\varepsilon). \tag{1}$$

The triplet depends on time τ and elliptic modulus $\varepsilon\in[0,1]$, where the elliptic modulus and complementary modulus $\delta\in[0,1]$ are related by the Pythagorean identity as follows:

$$\varepsilon^2+\delta^2=1. \tag{2}$$

If $\varepsilon\to 0_+$, then members of the first triplet approach the trigonometric asymptotes:

$$f(\tau,0)=\sin(\tau),\ \ g(\tau,0)=\cos(\tau),\ h(\tau,0)=1. \tag{3}$$

If $\varepsilon \to 1\_$, then members of the first triplet tend to the hyperbolic asymptotes:

$$f(\tau,1)=\tanh(\tau),\ g(\tau,1)=\operatorname{sech}(\tau),\ h(\tau,1)=\operatorname{sech}(\tau). \tag{4}$$

For the aim of clarity, we will typically drop argument τ and parameter ε in further results, *i.e.* a reduced form of the definition becomes

$$f=\mathrm{sn},\ g=\mathrm{cn},\ h=\mathrm{dn}. \tag{5}$$

From the viewpoint of the theory of dynamical systems, the first triplet is specified by the following system of Ordinary Differential Equations (ODEs) of the first order:

$$\frac{\mathrm{d}f}{\mathrm{d}\tau}=gh,\ \frac{\mathrm{d}g}{\mathrm{d}\tau}=-fh,\ \frac{\mathrm{d}h}{\mathrm{d}\tau}=-\varepsilon^2 fg, \tag{6}$$

where the first derivative of each member of the first triplet is proportional to a product of two comembers. So, the first triplet is complete with respect to differentiation of any order.

There are two independent algebraic relations between the squared members of the first triplet

$$\mathrm{cn}^2+\mathrm{sn}^2=1,\ \varepsilon^2\mathrm{sn}^2+\mathrm{dn}^2=1. \tag{7}$$

Using the independent algebraic relations and the Pythagorean identity for ε and δ, we compute a table of all algebraic relations between the squared members of the first triplet

$$\begin{aligned} &f^2+g^2=1, \quad f^2=1-g^2, \quad g^2=1-f^2,\\ &\varepsilon^2 f^2+h^2=1, \quad f^2=\frac{1-h^2}{\varepsilon^2}, \quad h^2=1-\varepsilon^2 f^2,\\ &-\varepsilon^2 g^2+h^2=\delta^2,\ g^2=\frac{h^2-\delta^2}{\varepsilon^2},\ h^2=\delta^2+\varepsilon^2 g^2. \end{aligned} \tag{8}$$

Therefore, only a single member from the first triplet is algebraically independent since two other members may be expressed via the single member by the above quadratic relations.

Taking the first derivative of the quadratic relations, we obtain that only a single member of the first triplet is differentially independent because

$$h\frac{\mathrm{d}h}{\mathrm{d}\tau}=\varepsilon^2 g\frac{\mathrm{d}g}{\mathrm{d}\tau}=-\varepsilon^2 f\frac{\mathrm{d}f}{\mathrm{d}\tau}=-\varepsilon^2 fgh, \tag{9}$$

in accordance with the dynamical definition of the first triplet.

2.2. Polynomial Potentials of the Fourth Order

Calculating squares of the dynamical definition of the first triplet, separating variables by the quadratic relations, factoring, expanding, and collecting like terms yields the following Hamiltonian ODEs:

$$K_{e,f}+P_{4,f}=E_{4,f}=0,\ K_{e,g}+P_{4,g}=E_{4,g}=0,\ K_{e,h}+P_{4,h}=E_{4,h}=0, \tag{10}$$

where

$$K_{e,f}=\frac{1}{2}\left(\frac{\mathrm{d}f}{\mathrm{d}\tau}\right)^2,\ K_{e,g}=\frac{1}{2}\left(\frac{\mathrm{d}g}{\mathrm{d}\tau}\right)^2,\ K_{e,h}=\frac{1}{2}\left(\frac{\mathrm{d}h}{\mathrm{d}\tau}\right)^2 \tag{11}$$

are kinetic energies of the Hamiltonian systems f, g, h with a unit mass,

$$P_{4,f} = -\frac{1}{2}(f-1)(f+1)(\varepsilon f-1)(\varepsilon f+1) = -\frac{\varepsilon^2}{2}f^4 + \frac{(\varepsilon^2+1)}{2}f^2 - \frac{1}{2}, \quad (12)$$

$$P_{4,g} = +\frac{1}{2}(g-1)(g+1)(\varepsilon^2 g^2+\delta^2) = +\frac{\varepsilon^2}{2}g^4 + \frac{(\delta^2-\varepsilon^2)}{2}g^2 - \frac{\delta^2}{2}, \quad (13)$$

$$P_{4,h} = +\frac{1}{2}(h-1)(h+1)(h-\delta)(h+\delta) = +\frac{1}{2}h^4 - \frac{(\delta^2+1)}{2}h^2 + \frac{\delta^2}{2} \quad (14)$$

are even polynomial potentials of the fourth order in f, g, h, respectively, and $E_{4,f}, E_{4,g}, E_{4,h}$ are vanishing total energies of f, g, h, correspondingly.

2.3. Polynomial Forces of the Third Order

We then take the first derivative of the dynamical definition of the first triplet, separate variables by the quadratic relations, factor, expand, and collect like terms to obtain the following Newtonian ODEs:

$$\frac{\mathrm{d}^2 f}{\mathrm{d}\tau^2} = F_{3,f}, \ \frac{\mathrm{d}^2 g}{\mathrm{d}\tau^2} = F_{3,g}, \ \frac{\mathrm{d}^2 h}{\mathrm{d}\tau^2} = F_{3,h}, \quad (15)$$

where

$$\frac{\mathrm{d}^2 f}{\mathrm{d}\tau^2}, \ \frac{\mathrm{d}^2 g}{\mathrm{d}\tau^2}, \ \frac{\mathrm{d}^2 h}{\mathrm{d}\tau^2} \quad (16)$$

are accelerations of f, g, h,

$$F_{3,f} = +\left(\sqrt{2}\,\varepsilon f - \sqrt{\varepsilon^2+1}\right) f \left(\sqrt{2}\,\varepsilon f + \sqrt{\varepsilon^2+1}\right) = +2\varepsilon^2 f^3 - (\varepsilon^2+1) f \quad (17)$$

is an odd third-order polynomial force in f,

$$F_{3,g} = -\left(\sqrt{2}\,\varepsilon g - \sqrt{\varepsilon^2-\delta^2}\right) g \left(\sqrt{2}\,\varepsilon g + \sqrt{\varepsilon^2-\delta^2}\right) = -2\varepsilon^2 g^3 + (\varepsilon^2-\delta^2) g \quad (18)$$

is an odd third-order polynomial force in g for $\sqrt{2}/2 \le \varepsilon \le 1$,

$$F_{3,g} = -g\left(2\varepsilon^2 g^2 - \varepsilon^2 + \delta^2\right) = -2\varepsilon^2 g^3 + (\varepsilon^2-\delta^2) g \quad (19)$$

is an odd third-order polynomial force in g for $0 \le \varepsilon \le \sqrt{2}/2$,

$$F_{3,h} = -\left(\sqrt{2}\,h - \sqrt{\delta^2+1}\right) h \left(\sqrt{2}\,h + \sqrt{\delta^2+1}\right) = -2h^3 + (\delta^2+1) h \quad (20)$$

is an odd third-order polynomial force in h.

It is a straightforward procedure to verify that the polynomial forces of the third order are potential since they are connected with the polynomial potentials of the fourth order by the following relationships:

$$F_{3,f} = -\frac{\mathrm{d}P_{4,f}}{\mathrm{d}f}, \ F_{3,g} = -\frac{\mathrm{d}P_{4,g}}{\mathrm{d}g}, \ F_{3,h} = -\frac{\mathrm{d}P_{4,h}}{\mathrm{d}h}. \quad (21)$$

2.4. Static Visualizations

Polynomial force $F_{3,f}$, polynomial potential $P_{4,f}$, and the first Hamiltonian system f are shown in **Figure 1(a)**, **Figure 1(b)**, and **Figure 1(c)**, respectively, for

various values of ε. Blue solid curves correspond to a hyperbolic value of $\varepsilon = \varepsilon_h$, black dotted curves to a critical value of $\varepsilon = \varepsilon_c$, and green dashed curves to a trigonometric value of $\varepsilon = \varepsilon_t$, where

$$\varepsilon_t = 0.0000001,\ \varepsilon_c = \sqrt{2}/2 = 0.7071070,\ \varepsilon_h = 0.9999999. \tag{22}$$

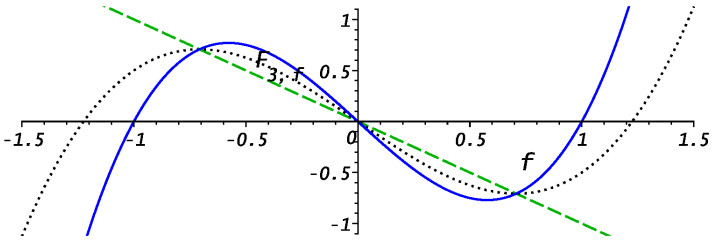

(a)

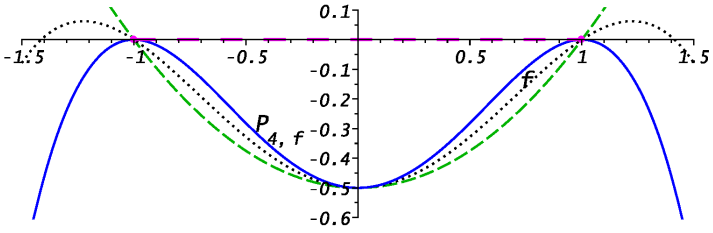

(b)

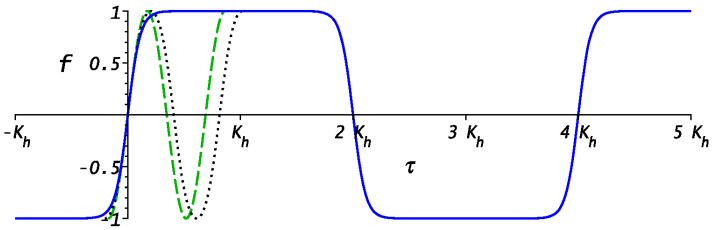

(c)

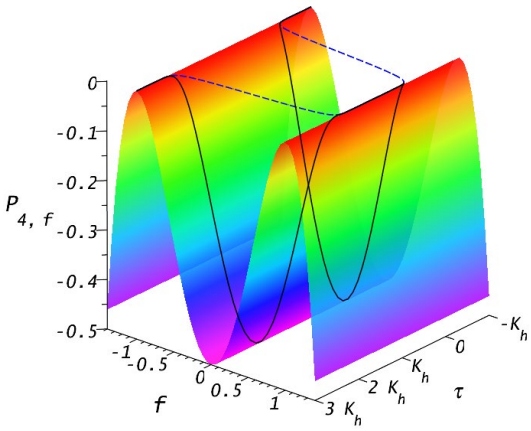

(d)

Figure 1. Plots of the first Hamiltonian system: (a) $-F_{3,f}$, (b) $-P_{4,f}$,(c) $-f$ for various values of $\varepsilon : \varepsilon_t, \varepsilon_c, \varepsilon_h$, (d) the last frame of the animated 3-d Hamiltonian map of $f(\tau, \varepsilon_h)$ on the surface of polynomial potential $P_{4,f}(f, \tau, \varepsilon_h)$.

The correspondent values of the complete elliptic integral of the first kind $K = K(\varepsilon)$ [8] are following:

$$K_t = K(\varepsilon_t) = 1.5707963,\ K_c = K(\varepsilon_c) = 1.8540747,\ K_h = K(\varepsilon_h) = 9.0987690. \quad (23)$$

In Figure 1(c), f is shown using the green dashed curve and the black dotted curve on domains $[-K_t, 5K_t]$ and $[-K_c, 5K_c]$, respectively.

Calculation of three zeros of $F_{3,f}$ gives

$$f_{F,1} = -\frac{\sqrt{2(\varepsilon^2+1)}}{2\varepsilon},\ f_{F,2} = 0,\ f_{F,3} = +\frac{\sqrt{2(\varepsilon^2+1)}}{2\varepsilon}. \quad (24)$$

As ε varies from 0 to 1, $f_{F,1}$ moves from $-\infty$ to -1, $f_{F,2}$ is stationary, and $f_{F,3}$ moves from $+\infty$ to $+1$ since $F_{3,f}$ transforms from a linear polynomial $-f$ into the cubic polynomial.

In agreement with the first derivative of the polynomial potentials, zeros of $F_{3,f}$ correspond to extrema of $P_{4,f}$. Namely, there are the first local maximum, the local minimum, and the second local maximum that are given by

$$P_{4,f,\max,1} = \frac{(\varepsilon^2-1)^2}{8\varepsilon^2},\ P_{4,f,\min} = -\frac{1}{2},\ P_{4,f,\max,2} = \frac{(\varepsilon^2-1)^2}{8\varepsilon^2}. \quad (25)$$

As ε varies from 0 to 1, $P_{4,f,\max,1}$ at $f = f_{F,1}$ and $P_{4,f,\max,2}$ at $f = f_{F,3}$ change from ∞ to 0 and $P_{4,f,\min}$ at $f = f_{F,2}$ remains constant since $P_{4,f}$ transforms from a quadratic polynomial $(f^2-1)/2$ into the fourth-order polynomial.

Four zeros of $P_{4,f}$ are computed as follows:

$$f_1 = -\frac{1}{\varepsilon},\ f_2 = -1,\ f_3 = +1,\ f_4 = +\frac{1}{\varepsilon}. \quad (26)$$

As ε varies from 0 to 1, f_1 moves from -∞ to -1, $f_2 = f_{\min} = -1$ and $f_3 = f_{\max} = +1$ are steady, and f_4 moves from +∞ to +1 since $P_{4,f}$ alters the order from two to four.

Depth of the sn-potential well

$$d_{4,f} = P_{4,f,\max,2} - P_{4,f,\min} = \frac{(\varepsilon^2+1)^2}{8\varepsilon^2} \quad (27)$$

and width of the sn-potential well

$$w_{4,f} = f_{F,3} - f_{F,1} = \frac{\sqrt{2(\varepsilon^2+1)}}{\varepsilon}. \quad (28)$$

Thus, the first Hamiltonian system $f \in [f_{\min}, f_{\max}] = [-1, +1]$ is locked in the sn-potential well $[f_{F,1}, f_{F,3}]$. The vanishing total energy $E_{4,f}$ of f is indicated in Figure 1(b) by a space dashed magenta line and the ultimate positions of f are specified by magenta dots. As $\varepsilon \to 1_-$, f approaches the nonlinear sn-oscillation with positive pulses of a rectangular shape for $4nK(\varepsilon) \le \tau \le 2K(\varepsilon) + 4nK(\varepsilon)$ and negative pulses of a rectangular shape for $2K(\varepsilon) + 4nK(\varepsilon) \le \tau \le 4K(\varepsilon) + 4nK(\varepsilon)$,

where $n=0,\pm1,\pm2,\cdots$ is an integer. For $\varepsilon=\varepsilon_h$, the shape of rectangular pulses coincides with the graph accuracy with $\tanh(\tau)$ for $-K(\varepsilon)+4nK(\varepsilon)\le\tau\le K(\varepsilon)+4nK(\varepsilon)$ and with $-\tanh(\tau)$ for $K(\varepsilon)+4nK(\varepsilon)\le\tau\le 3K(\varepsilon)+4nK(\varepsilon)$.

The period of the sn-oscillation is $4K(\varepsilon)$ since periodic minimums $f_{\min}=f(\tau_{\min})=-1$ and periodic maximums $f_{\max}=f(\tau_{\max})=+1$ are reached at

$$\tau_{\min}=-K(\varepsilon)+4nK(\varepsilon),\quad \tau_{\max}=+K(\varepsilon)+4nK(\varepsilon). \tag{29}$$

The zeros of f are periodic points of inflection $f_{\inf}=f(\tau_{\inf})=f_{F,2}=0$, which the first Hamiltonian system attains at

$$\tau_{\inf}=2nK(\varepsilon). \tag{30}$$

Polynomial force $F_{3,g}$, polynomial potential $P_{4,g}$, and the second Hamiltonian system g are visualized in Figure 2(a), Figure 2(b), and Figure 2(c), correspondingly.

Calculation of three zeros of $F_{3,g}$ gives

$$g_{F,1}=-\frac{\sqrt{2\left(\varepsilon^2-\delta^2\right)}}{2\varepsilon},\quad g_{F,2}=0,\quad g_{F,3}=+\frac{\sqrt{2\left(\varepsilon^2-\delta^2\right)}}{2\varepsilon}. \tag{31}$$

As ε varies from 0 to 1, $g_{F,1}$ moves from $-\mathrm{I}\infty$ to $-\sqrt{2}/2$, $g_{F,2}$ is stationary, and $g_{F,3}$ moves from $+\mathrm{I}\infty$ to $+\sqrt{2}/2$ since $F_{3,g}$ transforms from a linear polynomial $-g$ into the cubic polynomial, where I is the imaginary unit. All imaginary roots become real for $\varepsilon=\varepsilon_c$ as $g_{F,1}=g_{F,2}=g_{F,3}=0$.

In the view of the first derivative of the polynomial potentials, zeros of $F_{3,g}$ produce extrema of $P_{4,g}$. Specifically, the first local minimum, the local maximum, and the second local minimum are computed by

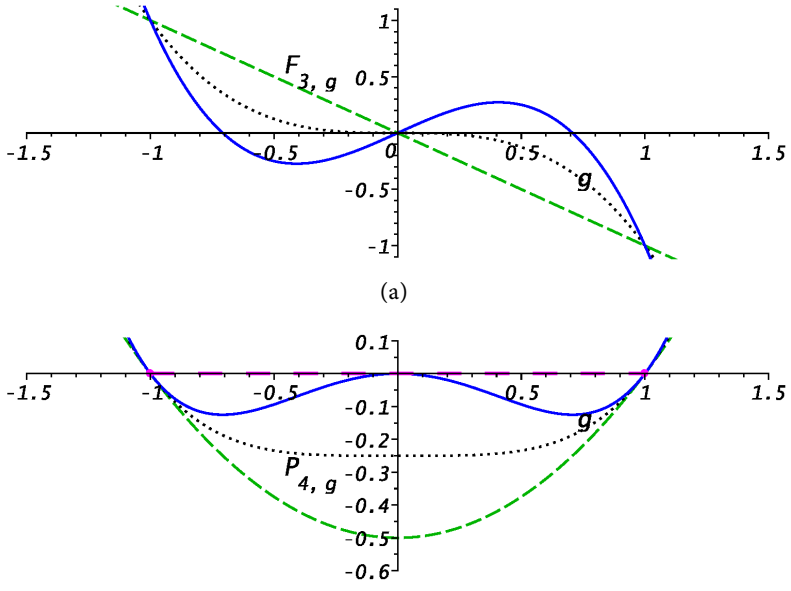

(a)

(b)

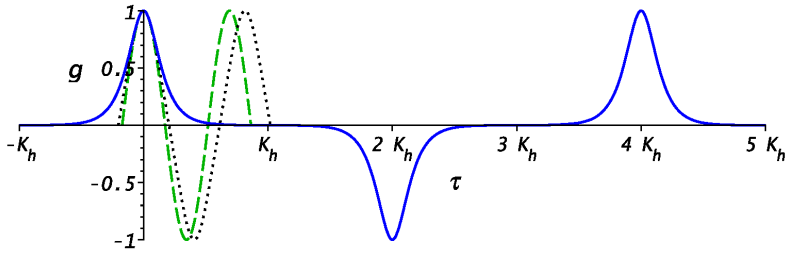

(c)

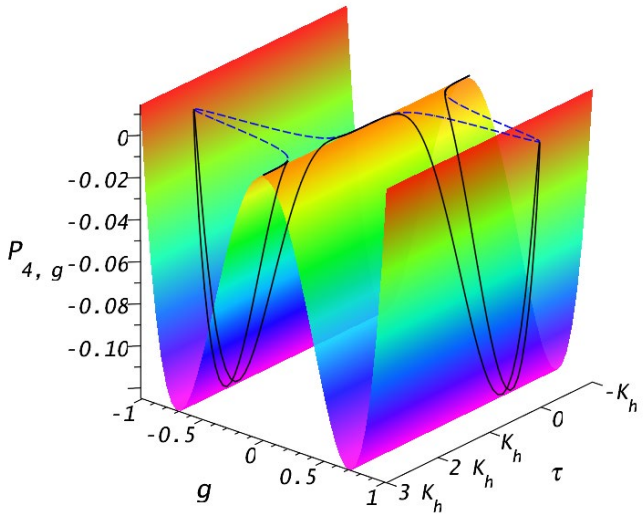

(d)

Figure 2. Plots of the second Hamiltonian system: (a) $-F_{3,g}$, (b) $-P_{4,g}$, (c) $-g$ for various values of $\varepsilon : \varepsilon_t, \varepsilon_c, \varepsilon_h$, (d) the last frame of the animated 3-d Hamiltonian map of $g(\tau, \varepsilon_h)$ on the surface of polynomial potential $P_{4,g}(g, \tau, \varepsilon_h)$.

$$P_{4,g,\min,1} = -\frac{1}{8\varepsilon^2}, \quad P_{4,g,\max} = \frac{\varepsilon^2 - 1}{2}, \quad P_{4,g,\min,2} = -\frac{1}{8\varepsilon^2}. \tag{32}$$

As ε varies from ε_c to 1, $P_{4,g,\min,1}$ at $g = g_{F,1}$ and $P_{4,g,\min,2}$ at $g = g_{F,3}$ change from -1/4 to -1/8 and $P_{4,g,\max}$ at $g = g_{F,2}$ changes from -1/4 to 0 because $P_{4,g}$ transforms from a quadratic polynomial $\left(g^2 - 1\right)/2$ for $\varepsilon = 0$ into the fourth-order polynomial for $\varepsilon = 1$, while $P_{4,g,\min,1} = P_{4,g,\max} = P_{4,g,\min,2} = -1/4$ when $\varepsilon = \varepsilon_c$ as $P_{4,g}$ becomes $\left(g^4 - 1\right)/4$.

Four zeros of $P_{4,g}$ are calculated in the following form:

$$g_1 = -1, \quad g_2 = -\frac{\mathrm{I}\sqrt{1-\varepsilon^2}}{\varepsilon}, \quad g_3 = +\frac{\mathrm{I}\sqrt{1-\varepsilon^2}}{\varepsilon}, \quad g_4 = +1. \tag{33}$$

As ε varies from 0 to 1, g_1 and g_4 are stationary, g_2 moves from $-\mathrm{I}\infty$ to 0, and g_3 from $+\mathrm{I}\infty$ to 0, whereas $g_2 = -\mathrm{I}$ and $g_3 = +\mathrm{I}$ when $\varepsilon = \varepsilon_c$ because $P_{4,g}$ transforms into $\left(g^2 - 1\right)\left(g^2 + 1\right)/4$.

Depths of the cn-potential well at the locations of the local extrema $g_{F,1}$, $g_{F,2}$, and $g_{F,3}$ of $P_{4,g}$ for $\varepsilon > \varepsilon_c$ are

$$d_{4,g,1}=-P_{4,g,\min,1}=\frac{1}{8\varepsilon^2},\ d_{4,g,2}=-P_{4,g,\max}=\frac{1-\varepsilon^2}{2},\ d_{4,g,3}=-P_{4,g,\min,2}=\frac{1}{8\varepsilon^2},\quad (34)$$

respectively. A width of the cn-potential well does not depend on ε since

$$w_{4,g}=g_4-g_1=2. \quad (35)$$

The second Hamiltonian system $g\in\left[g_{\min},g_{\max}\right]=\left[-1,+1\right]$ oscillates in the cn-potential well $\left[g_1,g_4\right]$. The vanishing total energy $E_{4,g}$ of g is visualized in Figure 2(b) by a space dashed magenta line and the ultimate positions of g are shown by magenta dots. As $\varepsilon\to 1_-$, g approaches the nonlinear cn-oscillation with positive point pulses for $-K(\varepsilon)+4nK(\varepsilon)\le\tau\le K(\varepsilon)+4nK(\varepsilon)$ and negative point pulses for $K(\varepsilon)+4nK(\varepsilon)\le\tau\le 3K(\varepsilon)+4nK(\varepsilon)$. For $\varepsilon=\varepsilon_h$, the shape of point pulses coincides with the graph accuracy with $\operatorname{sech}(\tau)$ for $-K(\varepsilon)+4nK(\varepsilon)\le\tau\le K(\varepsilon)+4nK(\varepsilon)$ and with $-\operatorname{sech}(\tau)$ for $K(\varepsilon)+4nK(\varepsilon)\le\tau\le 3K(\varepsilon)+4nK(\varepsilon)$, which model the Dirac delta function.

The period of the cn-oscillation is $4K(\varepsilon)$ because periodic minimums $g_{\min}=g(\tau_{\min})=-1$ and periodic maximums $g_{\max}=g(\tau_{\max})=+1$ are attained at

$$\tau_{\min}=-2K(\varepsilon)+4nK(\varepsilon),\ \tau_{\max}=4nK(\varepsilon). \quad (36)$$

The zeros of g are again periodic points of inflection $g_{\inf}=g(\tau_{\inf})=g_{F,2}=0$, which g reaches at

$$\tau_{\inf}=K(\varepsilon)+2nK(\varepsilon). \quad (37)$$

Polynomial force $F_{3,h}$, polynomial potential $P_{4,h}$, and the third Hamiltonian system h are displayed in Figure 3(a), Figure 3(b), and Figure 3(c), sequentially.

We then calculate three zeros of $F_{3,h}$ and obtain

$$h_{F,1}=-\frac{\sqrt{2\left(2-\varepsilon^2\right)}}{2},\ h_{F,2}=0,\ h_{F,3}=+\frac{\sqrt{2\left(2-\varepsilon^2\right)}}{2}. \quad (38)$$

As ε varies from 0 to 1, $h_{F,1}$ moves from −1 to $-\sqrt{2}/2$, $h_{F,2}$ is stationary, and $h_{F,3}$ moves from +1 to $+\sqrt{2}/2$ because $F_{3,h}$ remains the cubic polynomial for all ε.

In the accordance with the first derivative of the polynomial potentials, zeros of $F_{3,h}$ correspond to extrema of $P_{4,h}$. Precisely, the first local minimum, the local maximum, and the second local minimum are given by

$$P_{4,h,\min,1}=-\frac{\varepsilon^4}{8},\ P_{4,h,\max}=\frac{1-\varepsilon^2}{2},\ P_{4,h,\min,2}=-\frac{\varepsilon^4}{8}. \quad (39)$$

As ε varies from 0 to 1, $P_{4,h,\min,1}$ at $h=h_{F,1}$ and $P_{4,h,\min,2}$ at $h=h_{F,3}$ change from 0 to −1/8 and $P_{4,h,\max}$ at $h=h_{F,2}$ changes from 1/2 to 0 since $P_{4,h}$ is the fourth-order polynomial for all ε.

Four zeros of $P_{4,h}$ are computed in the following form:

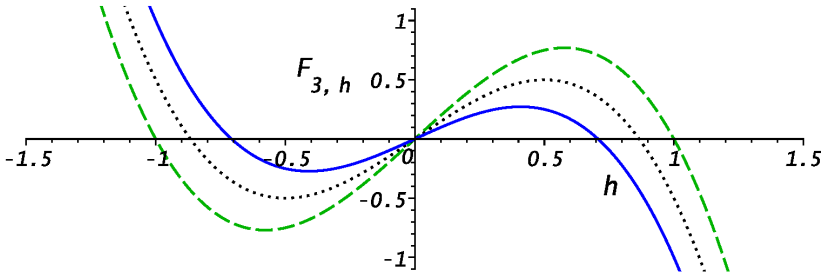

(a)

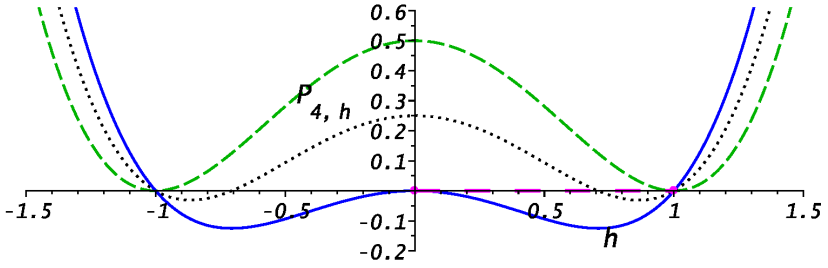

(b)

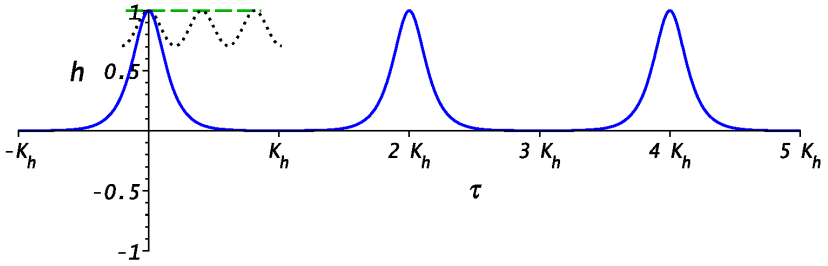

(c)

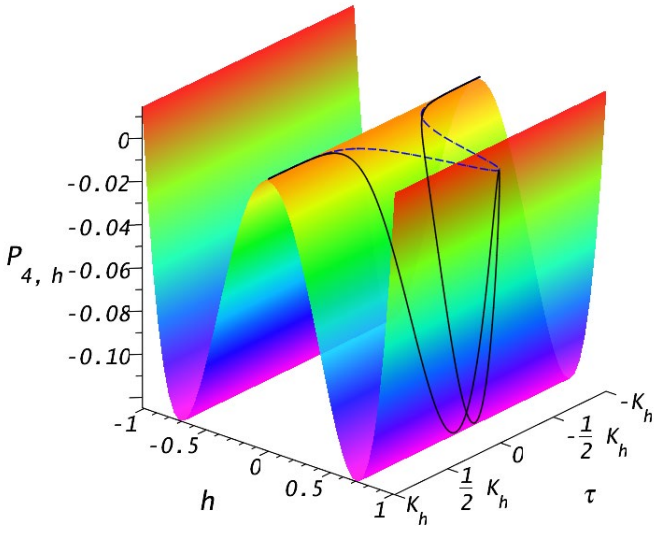

(d)

Figure 3. Plots of the third Hamiltonian system: (a) $-F_{3,h}$, (b) $-P_{4,h}$, (c) $-h$ for various values of $\varepsilon:\varepsilon_l,\varepsilon_c,\varepsilon_h$, (d) the last frame of the animated 3-d Hamiltonian map of $h(\tau,\varepsilon_h)$ on the surface of polynomial potential $P_{4,h}(h,\tau,\varepsilon_h)$.

$$h_1=-1,\ \ h_2=-\sqrt{1-\varepsilon^2},\ \ h_3=+\sqrt{1-\varepsilon^2},\ \ h_4=+1. \tag{40}$$

As ε varies from 0 to 1, h_1 and h_4 are stationary, h_2 moves from -1 to 0, and h_3 from +1 to 0 as $P_{4,h}$ has the same order for all ε.

Depth of the dn-potential well

$$d_{4,h}=P_{4,h,\max}-P_{4,h,\min,2}=\frac{\left(\varepsilon^2-2\right)^2}{8}. \tag{41}$$

Width of the dn-potential well

$$w_{4,h}=h_w=\sqrt{2-\varepsilon^2} \tag{42}$$

is a solution of the following algebraic equation:

$$P_{4,h}-P_{4,h,\max}-\frac{h^2\left(h^2-h_w^2\right)}{2}=0. \tag{43}$$

Contrary to the cn-potential well in **Figure 2(b)**, potential sub-wells in **Figure 3(b)** are separated since $P_{4,h,\max}=+\left(1-\varepsilon^2\right)/2>0$ and $P_{4,g,\max}=-\left(1-\varepsilon^2\right)/2<0$ at the origin. Therefore, a periodic motion of the third Hamiltonian system $h\in\left[h_{\min},h_{\max}\right]=\left[\sqrt{1-\varepsilon^2},+1\right]$ is bounded in the dn-potential well $\left[0,h_w\right]$. The total vanishing energy $E_{4,h}$ of h is displayed in **Figure 3(b)** using a space dashed magenta line and the ultimate positions of h are visualized by magenta dots. As $\varepsilon\to 1_-$, h tends to the nonlinear dn-pulsation with only positive point pulses for $-K\left(\varepsilon\right)+2nK\left(\varepsilon\right)\le\tau\le+K\left(\varepsilon\right)+2nK\left(\varepsilon\right)$. For $\varepsilon=\varepsilon_h$, the shape of point pulses co-incides with the graph accuracy with $\operatorname{sech}\left(\tau\right)$ for $-K\left(\varepsilon\right)+2nK\left(\varepsilon\right)\le\tau\le+K\left(\varepsilon\right)+2nK\left(\varepsilon\right)$.

The period of the dn-pulsation is $2K\left(\varepsilon\right)$ since periodic minimums $h_{\min}=h\left(\tau_{\min}\right)=\sqrt{1-\varepsilon^2}$ and periodic maximums $h_{\max}=h\left(\tau_{\max}\right)=1$ are attained at

$$\tau_{\min}=-K\left(\varepsilon\right)+2nK\left(\varepsilon\right),\ \ \tau_{\max}=2nK\left(\varepsilon\right). \tag{44}$$

The third Hamiltonian system does not have zeros since h is strictly positive.

2.5. Dynamic Visualizations

From the viewpoint of the Hamiltonian dynamics, a Hamiltonian system of the first triplet

$$\phi=\left[f,g,h\right] \tag{45}$$

is a solution of the Hamiltonian ODE

$$K_{e,\phi}+P_{4,\phi}=E_{4,\phi}=\frac{1}{2}\left(\frac{\mathrm{d}\phi}{\mathrm{d}\tau}\right)^2+\sigma_4\phi^4+\sigma_2\phi^2+\sigma_0=0, \tag{46}$$

where $K_{e,\phi}$ is the kinetic energy, $P_{4,\phi}$ is the even polynomial potential in ϕ of the fourth order, total energy $E_{4,\phi}=0$, and polynomial coefficients of f,g,h are

$$[\sigma_4,\sigma_2,\sigma_0]=\left[-\varepsilon^2/2,\left(\varepsilon^2+1\right)/2,-1/2\right], \tag{47}$$

$$[\sigma_4,\sigma_2,\sigma_0]=\left[+\varepsilon^2/2,\left(\delta^2-\varepsilon^2\right)/2,-\delta^2/2\right], \tag{48}$$

$$[\sigma_4,\sigma_2,\sigma_0]=\left[+1/2,-\left(\delta^2+1\right)/2,+\delta^2/2\right], \tag{49}$$

respectively.

From the perspective of the Newtonian dynamics, ϕ represents a solution of the Newtonian ODE

$$\frac{\mathrm{d}^2\phi}{\mathrm{d}\tau^2}=F_{3,\phi}=\omega_3\phi^3+\omega_1\phi, \tag{50}$$

where the second derivative of ϕ is the acceleration, $F_{3,\phi}$ is the odd polynomial force in ϕ of the third order, and polynomial coefficients of f,g,h are

$$[\omega_3,\omega_1]=\left[+2\varepsilon^2,-\left(\varepsilon^2+1\right)\right], \tag{51}$$

$$[\omega_3,\omega_1]=\left[-2\varepsilon^2,+\left(\varepsilon^2-\delta^2\right)\right], \tag{52}$$

$$[\omega_3,\omega_1]=\left[-2,+\left(\delta^2+1\right)\right], \tag{53}$$

correspondingly.

The polynomial force is connected with the polynomial potential by the following relations:

$$F_{3,\phi}=-\frac{\mathrm{d}P_{4,\phi}}{\mathrm{d}\phi},\ \omega_3=-4\sigma_4,\ \omega_1=-2\sigma_2. \tag{54}$$

The dynamical problems for the Hamiltonian or Newtonian ODEs are subjected to the following initial conditions for f,g,h, respectively:

$$f\big|_{\tau=0}=0,\ \left.\frac{\mathrm{d}f}{\mathrm{d}\tau}\right|_{\tau=0}=1, \tag{55}$$

$$g\big|_{\tau=0}=1,\ \left.\frac{\mathrm{d}g}{\mathrm{d}\tau}\right|_{\tau=0}=0, \tag{56}$$

$$h\big|_{\tau=0}=1,\ \left.\frac{\mathrm{d}h}{\mathrm{d}\tau}\right|_{\tau=0}=0. \tag{57}$$

Solutions of the Hamiltonian or Newtonian ODEs with these initial conditions provide unique solutions for the first triplet.

Figure 1(b) and Figure 1(c) are integrated for $\varepsilon=\varepsilon_h$ in a three-dimensional (3-d) Hamiltonian map animated on $\tau\in\left[-K_h,3K_h\right]$, the last frame of which is shown in Figure 1(d). A 3-d trajectory of the first Hamiltonian system $f\left(\tau,\varepsilon_h\right)$ on the surface of polynomial potential $P_{4,f}\left(f,\tau,\varepsilon_h\right)$ is indicated by a black curve. A two-dimensional (2-d) projection of the 3-d trajectory on plane $\left[f,\tau\right]$ is visualized in Figure 1(d) by a blue dashed curve, which coincides with the 2-d trajectory of f displayed by the blue solid curve in Figure 1(c).

The periodic 3-d trajectory of f starts on the first potential barrier at $f=f_{\min}$ when $\tau=\tau_{\min}=-K_h+4nK_h$ and $K_{e,f}=-P_{4,f}=0$. As $P_{4,f}$

decreases towards the bottom of the sn-potential well, kinetic energy, $K_{e,f}=-P_{4,f}>0$, which determines the magnitude of system's velocity, initially increases and then decreases when the system transits in time interval $\tau\approx\left[-0.25K_h+4nK_h,+0.25K_h+4nK_h\right]$ from the first potential barrier to the second one at $f=f_{\max}$. The kinetic energy reaches its maximal value $K_{e,f}=-P_{4,f}=1/2$ at the bottom of the sn-potential well at $f=f_{\inf}$ when $\tau=\tau_{\inf}=2nK_h$. The first Hamiltonian system decelerates while moving along the potential barrier since $K_{e,f}\approx 0$ in time interval $\tau\approx\left[0.25K_h+4nK_h,1.75K_h+4nK_h\right]$, while $K_{e,f}=-P_{4,f}=0$ at $f=f_{\max}$ when $\tau=\tau_{\max}=+K_h+4nK_h$. Analogously, f primarily accelerates and sequentially decelerates in the sn-potential well and, finally, returns to the first potential barrier when $\tau\approx\left[1.75K_h+4nK_h,2.25K_h+4nK_h\right]$. The periodic 3-d trajectory finishes at $f=f_{\min}$ when $\tau=\tau_{\min}=3K_h+4nK_h$. The described details of the 3-d Hamiltonian map are clearly visualized in the animated **Figure 1(d)**.

In **Figure 2(d)**, the last frame of the animated 3-d Hamiltonian map on $\tau\in\left[-K_h,3K_h\right]$ combines for $\varepsilon=\varepsilon_h$ the 2-d polynomial potential in **Figure 2(b)** and the 2-d trajectory in **Figure 2(c)**. A black curve shows a 3-d trajectory of the second Hamiltonian system $g\left(\tau,\varepsilon_h\right)$ on the surface of polynomial potential $P_{4,g}\left(g,\tau,\varepsilon_h\right)$ and a blue dashed curve in **Figure 2(d)**, which coincides with the 2-d trajectory of g displayed by the blue solid curve in **Figure 2(c)**, presents a 2-d projection of the 3-d trajectory on plane $\left[g,\tau\right]$.

The periodic 3-d trajectory of g begins on the crest of the potential barrier at $g=g_{\inf}$ when $\tau=\tau_{\inf}=-K_h+2nK_h$ and $K_{e,g}=-P_{4,g}=\left(1-\varepsilon^2\right)/2$. As $P_{4,g}$ decreases in the first sub-well, where $g\in\left[0,1\right]$, kinetic energy, $K_{e,g}=-P_{4,g}>0$, initially increases towards the bottom of the first sub-well at $g=g_{F,3}$ and then decreases in time interval $\tau\approx\left[-0.50K_h+4nK_h,4nK_h\right]$. After reflection by the potential wall at $g=g_{\max}$ when $\tau=\tau_{\max}=4nK_h$ and $K_{e,g}=-P_{4,g}=0$, g again primarily accelerates and sequentially decelerates towards the potential barrier for $\tau\approx\left[4nK_h,0.50K_h+4nK_h\right]$, finishing this positive pulsation on the crest of the potential barrier at $g=g_{\inf}$ when $\tau=\tau_{\inf}=K_h+2nK_h$. The second Hamiltonian system then decelerates while moving along the potential barrier since $K_{e,g}\approx 0$ for $\tau\approx\left[0.50K_h+2nK_h,1.50K_h+2nK_h\right]$. Similarly to the positive pulsation, g consequently makes the negative pulsation in the second sub-well, where $g\in\left[-1,0\right]$, when $\tau\approx\left[1.50K_h+4nK_h,2.50K_h+4nK_h\right]$ due to the reflection from the potential wall at $g=g_{\min}$ when $\tau=\tau_{\min}=2K_h+4nK_h$ and $K_{e,g}=-P_{4,g}=0$. The periodic 3-d trajectory terminates at $g=g_{\inf}$ when $\tau=\tau_{\inf}=3K_h+2nK_h$. The specified features of the 3-d Hamiltonian map are unambiguously displayed in the animated **Figure 2(d)**.

In **Figure 3(d)**, the last frame of the 3-d Hamiltonian map animated on $\tau\in\left[-K_h,+K_h\right]$ synthesizes for $\varepsilon=\varepsilon_h$ **Figure 3(b)**, which contains the 2-d polynomial potential, with **Figure 3(c)**, which displays the 2-d trajectory. A black curve in **Figure 3(d)** shows a 3-d trajectory of the third Hamiltonian system

$h(\tau,\varepsilon_h)$ on the surface of polynomial potential $P_{4,h}(h,\tau,\varepsilon_h)$. A 2-d projection of the 3-d trajectory on plane $[h,\tau]$ is visualized in Figure 3(d) by a blue dashed curve, which coincides with the 2-d trajectory of h visualized with the help of the blue solid curve in Figure 3(c).

Similar to the positive pulsation in Figure 2(d), the periodic 3-d trajectory of h starts on the potential barrier at $h=h_{\min}$ when $\tau=\tau_{\min}=-K_h+2nK_h$ and $K_{e,h}=-P_{4,h}=0$. As $P_{4,h}$ decreases in the dn-potential well, kinetic energy, $K_{e,h}=-P_{4,h}>0$, initially increases towards the bottom of the dn-potential well and then decreases in time interval $\tau\approx[-0.50K_h+2nK_h,2nK_h]$. The kinetic energy reaches its maximal value $K_{e,h}=-P_{4,h}=\varepsilon^4/8$ at the bottom of the dn-potential well at $h=h_{F,3}$. The third Hamiltonian system is then reflected by the potential wall at $h=h_{\max}$ when $\tau=\tau_{\max}=2nK_h$ and $K_{e,h}=-P_{4,h}=0$. After the reflection, h once more primarily accelerates and sequentially decelerates towards the potential barrier for $\tau\approx[2nK_h,+0.50K_h+2nK_h]$, terminating this positive pulsation at the potential barrier. After the positive pulsation, h decelerates along the potential barrier when $\tau\approx[+0.50K_h+2nK_h,+1.50K_h+2nK_h]$ because then $K_{e,h}\approx 0$, whereas $K_{e,h}=-P_{4,h}=0$ on the potential barrier at the end of the periodic 3-d trajectory for $h=h_{\min}$ and $\tau=\tau_{\min}=K_h+2nK_h$. The mentioned aspects of the 3-d Hamiltonian map are obviously represented in the animated Figure 3(d).

3. Pulsatory Dynamic Models of the First Triplet Squared

3.1. Definitions of Elliptic Functions of the First Triplet Squared

We specify $[p,q,r](\tau,\varepsilon)$ as the first triplet of copolar elliptic functions squared $[\mathrm{sn}^2(\tau,\varepsilon),\ \mathrm{cn}^2(\tau,\varepsilon),\ \mathrm{dn}^2(\tau,\varepsilon)]$, correspondingly,

$$p(\tau,\varepsilon)=\mathrm{sn}^2(\tau,\varepsilon),\ q(\tau,\varepsilon)=\mathrm{cn}^2(\tau,\varepsilon),\ r(\tau,\varepsilon)=\mathrm{dn}^2(\tau,\varepsilon). \tag{58}$$

In agreement with the definition of the first triplet,

$$p(\tau,\varepsilon)=f^2(\tau,\varepsilon),\ q(\tau,\varepsilon)=g^2(\tau,\varepsilon),\ r(\tau,\varepsilon)=h^2(\tau,\varepsilon). \tag{59}$$

If $\varepsilon\to 0_+$, then trigonometric asymptotes of members of the first triplet squared become:

$$p(\tau,0)=\sin^2(\tau),\ q(\tau,0)=\cos^2(\tau),\ r(\tau,0)=1. \tag{60}$$

If $\varepsilon\to 1_-$, then hyperbolic asymptotes of members of the first triplet squared are

$$p(\tau,1)=\tanh^2(\tau),\ q(\tau,1)=\mathrm{sech}^2(\tau),\ r(\tau,1)=\mathrm{sech}^2(\tau). \tag{61}$$

For the aim of conciseness, we will further omit argument τ and parameter ε in computed results, *viz.* a simplified form of the definition of the first triplet squared is

$$p=f^2,\ q=g^2,\ r=h^2. \tag{62}$$

In agreement with the theory of dynamical systems, the triplet squared is

determined by the following system of ODEs of the first order:

$$\frac{\mathrm{d}p}{\mathrm{d}\tau}=2fgh,\ \frac{\mathrm{d}q}{\mathrm{d}\tau}=-2fgh,\ \frac{\mathrm{d}r}{\mathrm{d}\tau}=-2\varepsilon^2 fgh, \tag{63}$$

where the first derivative of each member of the triplet squared is proportional to a product of all members of the triplet. Contrary to the first triplet, the first triplet squared is opened with respect to differentiation of the first order.

With the help of the identities for the squared members of the first triplet and the squares of ε and δ, a table of all algebraic relations between members of the first triplet squared takes the following form:

$$\begin{aligned} &p+q=1, \quad p=1-q, \quad q=1-p,\\ &\varepsilon^2 p+r=1, \quad p=\frac{1-r}{\varepsilon^2}, \quad r=1-\varepsilon^2 p,\\ &-\varepsilon^2 q+r=\delta^2, \quad q=\frac{r-\delta^2}{\varepsilon^2}, \quad r=\delta^2+\varepsilon^2 q. \end{aligned} \tag{64}$$

Consequently, only a single member from the first triplet squared is algebraically independent since two other members may be computed in terms of the single member using the above linear relations.

We take the first derivative of the linear relations to show that only a single member of the first triplet squared is differentially independent since

$$\frac{\mathrm{d}r}{\mathrm{d}\tau}=\varepsilon^2\frac{\mathrm{d}q}{\mathrm{d}\tau}=-\varepsilon^2\frac{\mathrm{d}p}{\mathrm{d}\tau}=-2\varepsilon^2 fgh, \tag{65}$$

in agreement with the dynamical definition of the first triplet squared.

3.2. Polynomial Potentials of the Third Order

We then compute squares of the dynamical definition of the first triplet squared, separate variables by the linear relations, expand, and collect like terms to find the following Hamiltonian ODEs:

$$K_{e,p}+P_{3,p}=E_{3,p}=0,\ K_{e,q}+P_{3,q}=E_{3,q}=0,\ K_{e,r}+P_{3,r}=E_{3,r}=0, \tag{66}$$

where

$$K_{e,p}=\frac{1}{2}\left(\frac{\mathrm{d}p}{\mathrm{d}\tau}\right)^2,\ K_{e,q}=\frac{1}{2}\left(\frac{\mathrm{d}q}{\mathrm{d}\tau}\right)^2,\ K_{e,r}=\frac{1}{2}\left(\frac{\mathrm{d}r}{\mathrm{d}\tau}\right)^2 \tag{67}$$

are kinetic energies of the Hamiltonian systems p,q,r with a unit mass,

$$P_{3,p}=-2(p-1)\left(\varepsilon^2 p-1\right)p=-2\varepsilon^2 p^3+2\left(\varepsilon^2+1\right)p^2-2p, \tag{68}$$

$$P_{3,q}=+2(q-1)q\left(\varepsilon^2 q+\delta^2\right)=+2\varepsilon^2 q^3+2\left(\delta^2-\varepsilon^2\right)q^2-2\delta^2 q, \tag{69}$$

$$P_{3,r}=+2(r-1)\left(r-\delta^2\right)r=+2r^3-2\left(\delta^2+1\right)r^2+2\delta^2 r \tag{70}$$

are polynomial potentials of the third order in p,q,r, correspondingly, and $E_{3,p},E_{3,q},E_{3,r}$ are vanishing total energies of p,q,r, respectively. Therefore, the first triplet squared becomes closed with respect to differentiation starting from the first-order derivatives squared.

3.3. Polynomial Forces of the Second Order

Taking the first derivative of the dynamical definition of the first triplet squared, substituting the first derivatives of the first triple, separating variables by the quadratic relations, collecting like terms, using the definition of the first triple squared, and factoring yield the following Newtonian ODEs:

$$\frac{\mathrm{d}^2 p}{\mathrm{d}\tau^2} = F_{2,p},\ \frac{\mathrm{d}^2 q}{\mathrm{d}\tau^2} = F_{2,q},\ \frac{\mathrm{d}^2 r}{\mathrm{d}\tau^2} = F_{2,r}, \tag{71}$$

where

$$\frac{\mathrm{d}^2 p}{\mathrm{d}\tau^2},\ \frac{\mathrm{d}^2 q}{\mathrm{d}\tau^2},\ \frac{\mathrm{d}^2 r}{\mathrm{d}\tau^2} \tag{72}$$

are accelerations of p, q, r,

$$\begin{aligned} F_{2,p} &= +\frac{2}{3\varepsilon^2}\left(3\varepsilon^2 p - \varepsilon^2 - 1 - \sqrt{\varepsilon^4 - \varepsilon^2 + 1}\right)\left(3\varepsilon^2 p - \varepsilon^2 - 1 + \sqrt{\varepsilon^4 - \varepsilon^2 + 1}\right) \\ &= +6\varepsilon^2 p^2 - 4\left(\varepsilon^2 + 1\right)p + 2 \end{aligned} \tag{73}$$

is a second-order polynomial force in p,

$$\begin{aligned} F_{2,q} &= -\frac{2}{3\varepsilon^2}\left(3\varepsilon^2 q - \varepsilon^2 + \delta^2 - \sqrt{\varepsilon^4 + \varepsilon^2\delta^2 + \delta^4}\right)\left(3\varepsilon^2 q - \varepsilon^2 + \delta^2 + \sqrt{\varepsilon^4 + \varepsilon^2\delta^2 + \delta^4}\right) \\ &= -6\varepsilon^2 q^2 + 4\left(\varepsilon^2 - \delta^2\right)q + 2\delta^2 \end{aligned} \tag{74}$$

is a second-order polynomial force in q,

$$\begin{aligned} F_{2,r} &= -\frac{2}{3}\left(3r - \delta^2 - 1 - \sqrt{\delta^4 - \delta^2 + 1}\right)\left(3r - \delta^2 - 1 + \sqrt{\delta^4 - \delta^2 + 1}\right) \\ &= -6r^2 + 4\left(\delta^2 + 1\right)r - 2\delta^2 \end{aligned} \tag{75}$$

is a second-order polynomial force in r.

Similarly to the first triple, the polynomial forces are related with the polynomial potentials of the first triple squared by the following relations:

$$F_{2,p} = -\frac{\mathrm{d}P_{3,p}}{\mathrm{d}p},\ F_{2,q} = -\frac{\mathrm{d}P_{3,q}}{\mathrm{d}q},\ F_{3,r} = -\frac{\mathrm{d}P_{3,r}}{\mathrm{d}r}. \tag{76}$$

3.4. Static Visualizations

Polynomial force $F_{2,p}$, polynomial potential $P_{3,p}$, and the first Hamiltonian system squared p are shown in **Figure 4(a)**, **Figure 4(b)**, and **Figure 4(c)**, respectively, for various values of ε.

Computation of two zeros of $F_{2,p}$ yields

$$p_{F,1} = \frac{\varepsilon^2 + 1 - \sqrt{\varepsilon^4 - \varepsilon^2 + 1}}{3\varepsilon^2},\quad p_{F,2} = \frac{\varepsilon^2 + 1 + \sqrt{\varepsilon^4 - \varepsilon^2 + 1}}{3\varepsilon^2}. \tag{77}$$

As ε varies from 0 to 1, $p_{F,1}$ moves from 1/2 to 1/3 and $p_{F,2}$ moves from $+\infty$ to $+1$ since $F_{2,p}$ transforms from a linear polynomial $-4p+2$ into the quadratic polynomial.

In accordance with the first derivative of the polynomial potentials, zeros of $F_{2,p}$ correlate with extrema of $P_{3,p}$. Specifically, there are the local minimum and the local maximum that are computed by

$$P_{3,p,\min} = +\frac{2}{27\varepsilon^4}\left(R_\varepsilon - \varepsilon^2 - 1\right)\left(R_\varepsilon - \varepsilon^2 + 2\right)\left(R_\varepsilon + 2\varepsilon^2 - 1\right),$$
$$P_{3,p,\max} = -\frac{2}{27\varepsilon^4}\left(R_\varepsilon + \varepsilon^2 + 1\right)\left(R_\varepsilon + \varepsilon^2 - 2\right)\left(R_\varepsilon - 2\varepsilon^2 + 1\right), \tag{78}$$

where

$$R_\varepsilon = \sqrt{\varepsilon^4 - \varepsilon^2 + 1}. \tag{79}$$

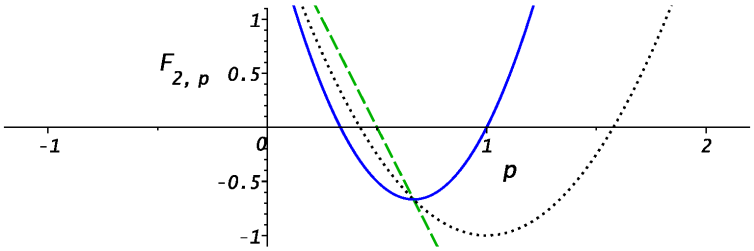

(a)

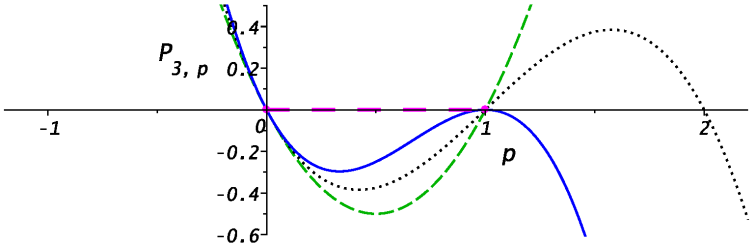

(b)

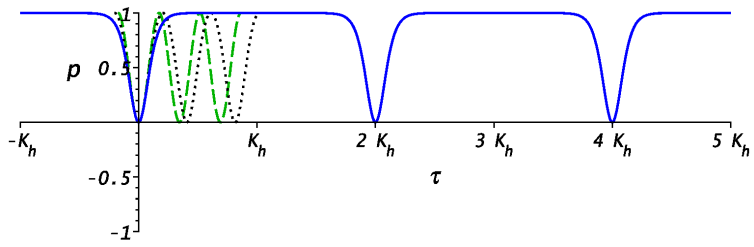

(c)

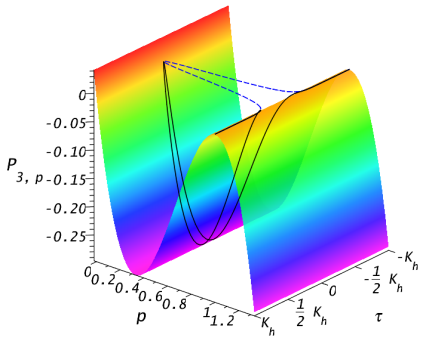

(d)

Figure 4. Plots of the first Hamiltonian system squared: (a) $-F_{2,p}$, (b) $-P_{3,p}$, (c) $-p$ for various values of $\varepsilon : \varepsilon_t, \varepsilon_c, \varepsilon_h$, (d) the last frame of the animated 3-d Hamiltonian map of $p(\tau, \varepsilon_h)$ on the surface of polynomial potential $P_{3,p}(p, \tau, \varepsilon_h)$.

As ε varies from 0 to 1, $P_{3,p,\min}$ at $p = p_{F,1}$ changes from $-1/2$ to $-8/27$ and $P_{3,p,\max}$ at $p = p_{F,2}$ from $+\infty$ to 0 since $P_{3,p}$ transforms from a quadratic polynomial $2p^2 - 2p$ into the third-order polynomial.

Three zeros of $P_{3,p}$ are calculated as follows:

$$p_1 = 0, \quad p_2 = 1, \quad p_3 = \frac{1}{\varepsilon^2}. \tag{80}$$

As ε varies from 0 to 1, $p_1 = p_{\min} = 0$ and $p_2 = p_{\max} = 1$ are steady, and p_3 moves from $+\infty$ to $+1$ since $P_{3,p}$ alters the order from two to three.

Depth of the sn^2-potential well

$$d_{3,p} = P_{3,p,\max} - P_{3,p,\min} = \frac{8R_\varepsilon^3}{27\varepsilon^4}. \tag{81}$$

Width of the sn^2-potential well

$$w_{4,p} = p_{F,2} - p_w = \frac{R_\varepsilon}{\varepsilon^2}, \tag{82}$$

where

$$p_w = \frac{\varepsilon^2 + 1 - 2R_\varepsilon}{3\varepsilon^2} \tag{83}$$

is a solution of the following algebraic equation:

$$P_{3,p} - P_{3,p,\max} + 2\varepsilon^2 (p - p_w)(p - p_{F,2})^2 = 0. \tag{84}$$

Thus, the first Hamiltonian system squared $p \in [p_{\min}, p_{\max}] = [0,1]$ is confined in the sn^2-potential well $[p_w, p_{F,2}]$. The vanishing total energy $E_{3,p}$ of p is displayed in **Figure 4(b)** by a space dashed magenta line and the ultimate positions of p are shown by magenta dots. As $\varepsilon \to 1_-$, p approaches the nonlinear sn^2-pulsation with positive pulses of a rectangular shape for $2nK(\varepsilon) \le \tau \le 2K(\varepsilon) + 2nK(\varepsilon)$. For $\varepsilon = \varepsilon_h$, the shape of rectangular pulses coincides with the graph accuracy with $\tanh^2(\tau)$ for $-K(\varepsilon) + 2nK(\varepsilon) \le \tau \le +K(\varepsilon) + 2nK(\varepsilon)$.

The period of the sn^2-pulsation is $2K(\varepsilon)$ since periodic minimums $p_{\min} = p(\tau_{\min}) = 0$ and periodic maximums $p_{\max} = p(\tau_{\max}) = 1$ are reached at

$$\tau_{\min} = 2nK(\varepsilon), \quad \tau_{\max} = K(\varepsilon) + 2nK(\varepsilon). \tag{85}$$

Polynomial force $F_{2,q}$, polynomial potential $P_{3,q}$, and the second Hamiltonian system squared q are represented in **Figure 5(a)**, **Figure 5(b)**, and **Figure 5(c)**, correspondingly.

Calculating two zeros of $F_{2,q}$, we have

$$q_{F,1} = \frac{2\varepsilon^2 - 1 - R_\varepsilon}{3\varepsilon^2}, \quad q_{F,2} = \frac{2\varepsilon^2 - 1 + R_\varepsilon}{3\varepsilon^2}. \tag{86}$$

As ε varies from 0 to 1, $q_{F,1}$ moves from $-\infty$ to 0 and $q_{F,2}$ from 1/2 to 2/3 since $F_{2,q}$ transforms from a linear polynomial $-4q + 2$ into the quadratic polynomial.

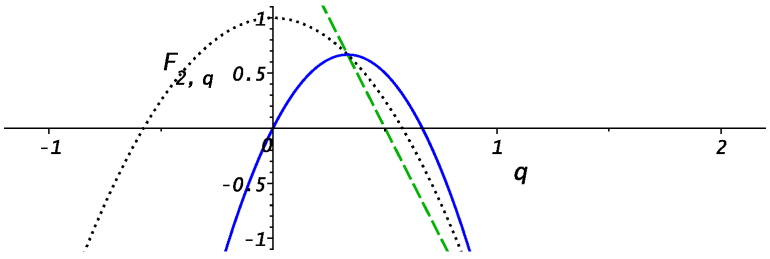

(a)

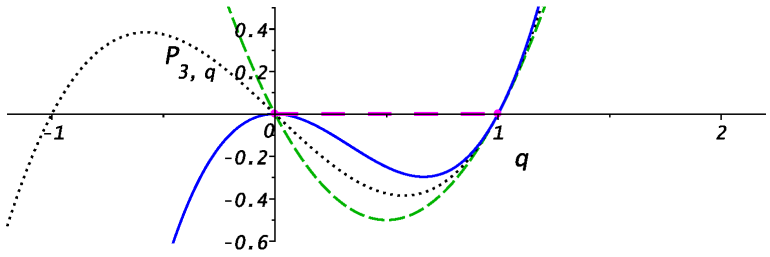

(b)

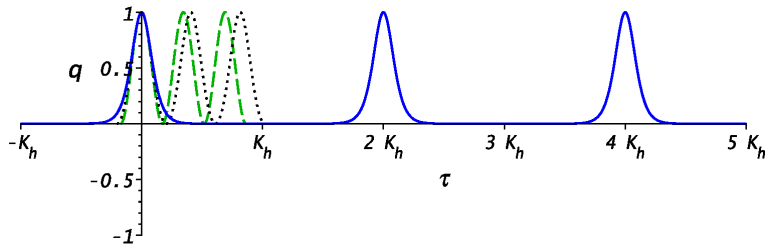

(c)

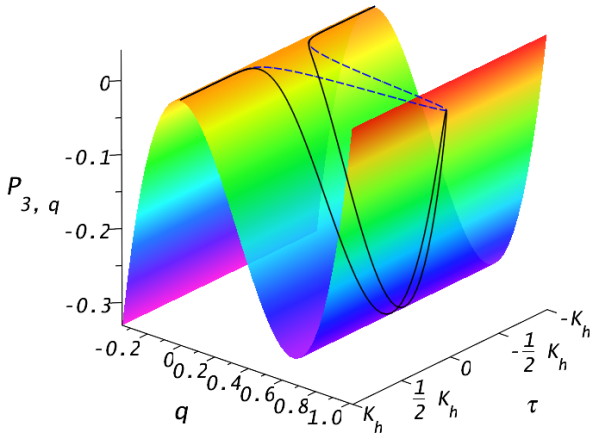

(d)

Figure 5. Plots of the second Hamiltonian system squared: (a) $-F_{2,q}$, (b) $-P_{3,q}$, (c) $-q$ for various values of $\varepsilon : \varepsilon_t, \varepsilon_c, \varepsilon_h$, (d) the last frame of the animated 3-d Hamiltonian map of $q(\tau, \varepsilon_h)$ on the surface of polynomial potential $P_{3,q}(q, \tau, \varepsilon_h)$.

In accordance with the first derivative of the polynomial potentials, zeros of $F_{2,q}$ correlate with extrema of $P_{3,q}$. Namely, the local maximum and the local minimum are obtained by

$$P_{3,q,\max}=-\frac{2}{27\varepsilon^4}\left(R_\varepsilon-2\varepsilon^2+1\right)\left(R_\varepsilon+\varepsilon^2-2\right)\left(R_\varepsilon+\varepsilon^2+1\right),$$
$$P_{3,q,\min}=+\frac{2}{27\varepsilon^4}\left(R_\varepsilon+2\varepsilon^2-1\right)\left(R_\varepsilon-\varepsilon^2+2\right)\left(R_\varepsilon-\varepsilon^2-1\right). \tag{87}$$

As ε varies from ε_c to 1, $P_{3,q,\max}$ at $q=q_{F,1}$ changes from $+\infty$ to 0 and $P_{3,q,\min}$ at $q=q_{F,2}$ from $-1/2$ to $-8/27$ since $P_{3,q}$ transforms from a quadratic polynomial $2q^2-2q$ to the third-order polynomial.

We then find three zeros of $P_{3,q}$ as follows:

$$q_1=\frac{1-\varepsilon^2}{\varepsilon^2},\quad q_2=0,\quad q_3=1. \tag{88}$$

As ε varies from 0 to 1, q_1 changes from $-\infty$ to 0, while $q_2=q_{\min}=0$ and $q_3=q_{\max}=1$ are stationary because $P_{3,q}$ alters the order from two to three.

Depth of the cn^2-potential well

$$d_{3,q}=P_{3,q,\max}-P_{3,q,\min}=\frac{8R_\varepsilon^3}{27\varepsilon^4}=d_{3,p}. \tag{89}$$

Width of the cn^2-potential well

$$w_{3,q}=q_w-q_{F,1}=\frac{R_\varepsilon}{\varepsilon^2}=w_{3,p}, \tag{90}$$

where

$$q_w=\frac{2\varepsilon^2-1+2R_\varepsilon}{3\varepsilon^2} \tag{91}$$

is a solution of the following algebraic equation:

$$P_{3,q}-P_{3,q,\max}-2\varepsilon^2\left(q-q_{F,1}\right)^2\left(q-q_w\right)=0. \tag{92}$$

So, the second Hamiltonian system squared $q\in\left[q_{\min},q_{\max}\right]=[0,1]$ pulsates in the cn^2-potential well $\left[q_{F,1},q_w\right]$. The vanishing total energy $E_{3,q}$ of q is visualized in Figure 5(b) by a space dashed magenta line and the ultimate positions of q are shown by magenta dots. As $\varepsilon\to 1_-$, q approaches the nonlinear cn^2-pulsation with positive point pulses for $-K(\varepsilon)+2nK(\varepsilon)\le\tau\le+K(\varepsilon)+2nK(\varepsilon)$. For $\varepsilon=\varepsilon_h$, the shape of point pulses coincides with the graph accuracy with $\operatorname{sech}^2(\tau)$ for $-K(\varepsilon)+2nK(\varepsilon)\le\tau\le+K(\varepsilon)+2nK(\varepsilon)$, which also models the Dirac delta function.

The period of the cn^2-pulsation is also $2K(\varepsilon)$ since periodic minimums $q_{\min}=q(\tau_{\min})=0$ and periodic maximums $q_{\max}=q(\tau_{\max})=1$ are reached at

$$\tau_{\min}=-K(\varepsilon)+2nK(\varepsilon),\quad \tau_{\max}=2nK(\varepsilon). \tag{93}$$

Polynomial force $F_{2,r}$, polynomial potential $P_{3,r}$, and the third Hamiltonian system squared r are given in Figure 6(a), Figure 6(b), and Figure 6(c), sequentially.

We then compute two zeros of $F_{2,r}$ and get

$$r_{F,1}=\frac{1}{3}\left(2-\varepsilon^2-R_\varepsilon\right),\quad r_{F,2}=r_{F,1}=\frac{1}{3}\left(2-\varepsilon^2+R_\varepsilon\right). \tag{94}$$

As ε varies from 0 to 1, $r_{F,1}$ moves from 1/3 to 0 and $r_{F,2}$ from 1 to 2/3 because $F_{2,r}$ remains the quadratic polynomial for all ε.

In agreement with the first derivative of the polynomial potentials, zeros of $F_{2,r}$ correspond to extrema of $P_{3,r}$. Precisely, the local maximum and the local minimum are returned by

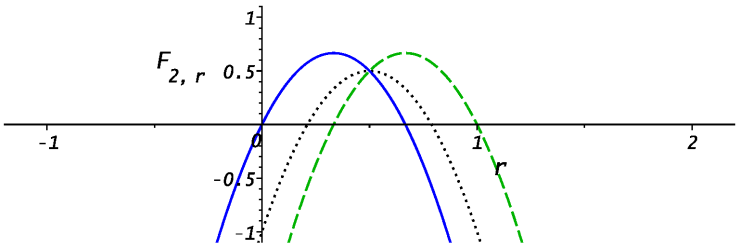

(a)

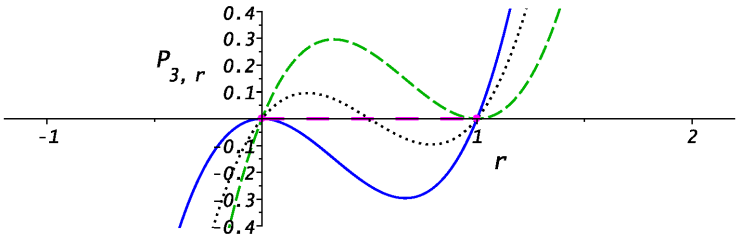

(b)

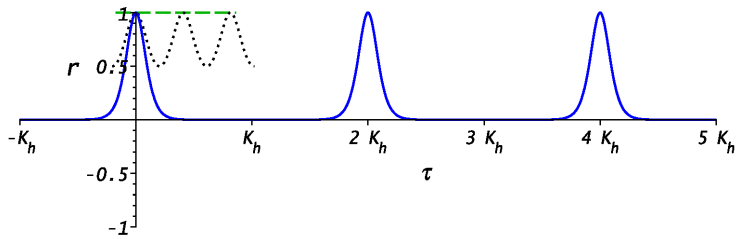

(c)

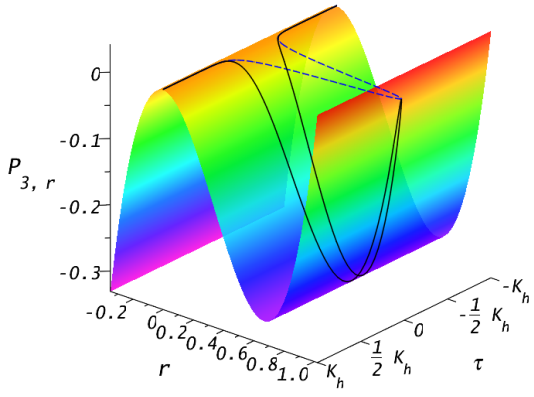

(d)

Figure 6. Plots of the third Hamiltonian system squared: (a) $-F_{2,r}$, (b) $-P_{3,r}$, (c) $-r$ for various values of $\varepsilon : \varepsilon_t, \varepsilon_c, \varepsilon_h$, (d) the last frame of the animated 3-d Hamiltonian map of $r(\tau, \varepsilon_h)$ on the surface of polynomial potential $P_{3,r}(r, \tau, \varepsilon_h)$.

$$P_{3,r,\max} = -\frac{2}{27}\left(R_\varepsilon - 2\varepsilon^2 + 1\right)\left(R_\varepsilon + \varepsilon^2 - 2\right)\left(R_\varepsilon + \varepsilon^2 + 1\right),$$
$$P_{3,r,\min} = +\frac{2}{27}\left(R_\varepsilon + 2\varepsilon^2 - 1\right)\left(R_\varepsilon - \varepsilon^2 + 2\right)\left(R_\varepsilon - \varepsilon^2 - 1\right). \tag{95}$$

As ε varies from 0 to 1, $P_{3,r,\max}$ at $r = r_{F,1}$ changes from +8/27 to 0 and $P_{3,r,\min}$ at $r = r_{F,2}$ from 0 to -8/27 since $P_{3,r}$ is the third-order polynomial for all ε.

We then find three zeroes of $P_{3,r}$ as

$$r_1 = 0, \quad r_2 = 1 - \varepsilon^2, \quad r_3 = 1. \tag{96}$$

As ε varies from 0 to 1, r_1 and $r_3 = r_{\max} = 1$ are stationary and $r_2 = r_{\min} = 1 - \varepsilon^2$ moves from 1 to 0 as $P_{3,r}$ has the same order for all ε.

Depth of the dn²-potential well

$$d_{3,r} = P_{3,r,\max} - P_{3,r,\min} = \frac{8R_\varepsilon^3}{27} = \varepsilon^4 d_{3,p} = \varepsilon^4 d_{3,q}. \tag{97}$$

Width of the dn²-potential well

$$w_{3,r} = r_w - r_{F,1} = R_\varepsilon = \varepsilon^2 w_{3,p} = \varepsilon^2 w_{3,q}, \tag{98}$$

where

$$r_w = \frac{1}{3}\left(2 - \varepsilon^2 + 2R_\varepsilon\right) \tag{99}$$

is a solution of the following algebraic equation:

$$P_{3,r} - P_{3,r,\max} - 2\left(r - r_{F,1}\right)^2\left(r - r_w\right) = 0. \tag{100}$$

Consequently, a periodic motion of the third Hamiltonian system squared $r \in \left[r_{\min}, r_{\max}\right] = \left[1 - \varepsilon^2, 1\right]$ with $E_{4,r} = 0$ is bounded in the dn²-potential well $\left[r_{F,1}, r_w\right]$. The total energy $E_{3,r}$ of r is shown in **Figure 6(b)** with the help of a space dashed magenta line and the ultimate positions of r are displayed by magenta dots. As $\varepsilon \to 1_-$, r approaches the nonlinear dn²-pulsation with positive point pulses for $-K(\varepsilon) + 2nK(\varepsilon) \le \tau \le +K(\varepsilon) + 2nK(\varepsilon)$. For $\varepsilon = \varepsilon_h$, the shape of point pulses coincides with the graph accuracy with $\operatorname{sech}^2(\tau)$ for $-K(\varepsilon) + 2nK(\varepsilon) \le \tau \le +K(\varepsilon) + 2nK(\varepsilon)$.

The period of the dn²-pulsation is $2K(\varepsilon)$, as well, since periodic minimums $r_{\min} = r(\tau_{\min}) = 1 - \varepsilon^2$ and periodic maximums $r_{\max} = r(\tau_{\max}) = 1$ are attained at

$$\tau_{\min} = -K(\varepsilon) + 2nK(\varepsilon), \quad \tau_{\max} = 2nK(\varepsilon). \tag{101}$$

3.5. Dynamic Visualizations

In terms of the Hamiltonian dynamics, a Hamiltonian system of the first triple squared

$$\phi = [p, q, r] \tag{102}$$

is a solution of the Hamiltonian ODE

$$K_{e,\phi}+P_{3,\phi}=E_{3,\phi}=\frac{1}{2}\left(\frac{\mathrm{d}\phi}{\mathrm{d}\tau}\right)^2+\sigma_3\phi^3+\sigma_2\phi^2+\sigma_1\phi=0, \tag{103}$$

where $K_{e,\phi}$ is the kinetic energy, $P_{3,\phi}$ is the polynomial potential in ϕ of the third order, total energy $E_{3,\phi}=0$, and polynomial coefficients of p,q,r are

$$[\sigma_3,\sigma_2,\sigma_1]=\left[-2\varepsilon^2,2\left(\varepsilon^2+1\right),-2\right], \tag{104}$$

$$[\sigma_3,\sigma_2,\sigma_1]=\left[+2\varepsilon^2,2\left(\delta^2-\varepsilon^2\right),-2\delta^2\right], \tag{105}$$

$$[\sigma_3,\sigma_2,\sigma_1]=\left[+2,-2\left(\delta^2+1\right),+2\delta^2\right], \tag{106}$$

respectively.

From the viewpoint of the Newtonian dynamics, ϕ is a solution of the Newtonian ODE

$$\frac{\mathrm{d}^2\phi}{\mathrm{d}\tau^2}=F_{2,\phi}=\omega_2\phi^3+\omega_1\phi+\omega_0, \tag{107}$$

where the second derivative of ϕ is the acceleration, $F_{2,\phi}$ is the polynomial force in ϕ of the second order, and polynomial coefficients of p,q,r are

$$[\omega_2,\omega_1,\omega_0]=\left[+6\varepsilon^2,-4\left(\varepsilon^2+1\right),+2\right], \tag{108}$$

$$[\omega_2,\omega_1,\omega_0]=\left[-6\varepsilon^2,-4\left(\delta^2-\varepsilon^2\right),+2\delta^2\right], \tag{109}$$

$$[\omega_2,\omega_1,\omega_0]=\left[-6,+4\left(\delta^2+1\right),-2\delta^2\right], \tag{110}$$

sequentially.

Analogous to the first triplet, the polynomial forces are related with the polynomial potentials of the first triplet squared by the following connections:

$$F_{2,\phi}=-\frac{\mathrm{d}P_{3,\phi}}{\mathrm{d}\phi},\ \omega_2=-3\sigma_3,\ \omega_1=-2\sigma_2,\ \omega_0=-\sigma_1. \tag{111}$$

The dynamical problems for the Hamiltonian or Newtonian ODEs are complemented by the following initial conditions for p,q,r, respectively:

$$p\big|_{\tau=0}=0,\ \left.\frac{\mathrm{d}p}{\mathrm{d}\tau}\right|_{\tau=0}=0, \tag{112}$$

$$q\big|_{\tau=0}=1,\ \left.\frac{\mathrm{d}q}{\mathrm{d}\tau}\right|_{\tau=0}=0, \tag{113}$$

$$r\big|_{\tau=0}=1,\ \left.\frac{\mathrm{d}r}{\mathrm{d}\tau}\right|_{\tau=0}=0. \tag{114}$$

Solutions of the Hamiltonian or Newtonian ODEs with the above initial conditions return unique solutions for the first triplet squared.

Figure 4(b) and Figure 4(c) are combined for $\varepsilon=\varepsilon_h$ in a 3-d Hamiltonian map animated on $\tau\in\left[-K_h,+K_h\right]$, the last frame of which is displayed in Figure 4(d). A 3-d trajectory of the first Hamiltonian system squared $p\left(\tau,\varepsilon_h\right)$ on the surface of polynomial potential $P_{3,p}\left(p,\tau,\varepsilon_h\right)$ is visualized by a black curve. A 2-d projection of the 3-d trajectory on plane $\left[p,\tau\right]$ is shown in Figure 4(d) by a

blue dashed curve, which coincides with the 2-d trajectory of p indicated by the blue solid curve in Figure 4(c).

The periodic 3-d trajectory of p begins on the potential barrier at $p = p_{\max}$ when $\tau = \tau_{\max} = -K_h + 2nK_h$ and $K_{e,p} = -P_{3,p} = 0$. As $P_{3,p}$ decreases in the sn^2-potential well, kinetic energy, $K_{e,p} = -P_{3,p} > 0$, initially increases towards the bottom of the sn^2-potential well at $p = p_{F,1}$ and then decreases in time interval $\tau \approx [-0.33K_h + 2nK_h, 2nK_h]$. The kinetic energy reaches its maximal value $K_{e,p,\max} = -P_{3,p,\min}$ at the bottom of the sn^2-potential well. After reflection by the potential wall at $p = p_{\min}$ when $\tau = \tau_{\min} = 2nK_h$ and $K_{e,p} = -P_{3,p} = 0$, p again accelerates and then decelerates towards the potential barrier for $\tau \approx [2nK_h, +0.33K_h + 2nK_h]$. Further p decelerates moving along the potential barrier since $K_{e,p} \approx 0$ for $\tau \approx [0.33K_h + 2nK_h, 1.66K_h + 2nK_h]$. The periodic 3-d trajectory finishes at $p = p_{\max}$ when $\tau = \tau_{\max} = +K_h + 2nK_h$. The described properties of the 3-d Hamiltonian map are evidently displayed in the animated Figure 4(d).

In Figure 5(d), the last frame of the animated 3-d Hamiltonian map on $\tau \in [-K_h, +K_h]$ integrates for $\varepsilon = \varepsilon_h$ Figure 5(b), which contains the 2-d polynomial potential, with Figure 5(c), which displays the 2-d trajectory. A black curve in Figure 5(d) visualizes a 3-d trajectory of the second Hamiltonian system squared $q(\tau, \varepsilon_h)$ on the surface of the polynomial potential $P_{3,q}(q, \tau, \varepsilon_h)$. A blue dashed curve in Figure 5(d), which fits the 2-d trajectory of q shown by the blue solid curve in Figure 5(c), represents a 2-d projection of the 3-d trajectory on plane $[q, \tau]$.

The periodic 3-d trajectory of q starts on the potential barrier at $q = q_{\min}$ when $\tau = \tau_{\min} = -K_h + 2nK_h$ and $K_{e,q} = -P_{3,q} = 0$. As $P_{3,q}$ decreases in the cn^2-potential well, kinetic energy, $K_{e,q} = -P_{3,q} > 0$, initially increases towards the bottom of the cn^2-potential well and then decreases in time interval $\tau \approx [-0.33K_h + 2nK_h, 2nK_h]$. The kinetic energy reaches its maximal value $K_{e,q,\max} = -P_{3,q,\min}$ at the bottom of the cn^2-potential well at $q = q_{F,2}$. After reflection by the potential wall at $q = q_{\max}$ when $\tau = \tau_{\max} = 2nK_h$ and $K_{e,q} = -P_{3,q} = 0$, q once more primarily accelerates and sequentially decelerates towards the potential barrier for $\tau \approx [2nK_h, +0.33K_h + 2nK_h]$. Later q decelerates while moving along the potential barrier as $K_{e,q} \approx 0$ for $\tau \approx [0.33K_h + 2nK_h, 1.66K_h + 2nK_h]$. The periodic 3-d trajectory terminates at $q = q_{\min}$ when $\tau = \tau_{\min} = +K_h + 2nK_h$. The described details of the 3-d Hamiltonian map are clearly visualized by the animated Figure 5(d).

In Figure 6(d), the last frame of the 3-d Hamiltonian map animated on $\tau \in [-K_h, +K_h]$ synthesizes for $\varepsilon = \varepsilon_h$ the 2-d polynomial potential in Figure 6(b) and the 2-d trajectory in Figure 6(c). A black curve shows a 3-d trajectory of the third Hamiltonian system squared $r(\tau, \varepsilon_h)$ on the surface of the polynomial potential $P_{3,r}(r, \tau, \varepsilon_h)$ and a blue dashed curve in Figure 6(d), which coincides with the 2-d trajectory of r displayed by the blue solid curve in Figure 6(c),

presents a 2-d projection of the 3-d trajectory on plane $[r,\tau]$.

The periodic 3-d trajectory of r begins on the potential barrier at $r=r_{\min}$ when $\tau=\tau_{\min}=-K_h+2nK_h$ and $K_{e,r}=-P_{3,r}=0$. As $P_{3,r}$ decreases in the dn^2-potential well, kinetic energy, $K_{e,r}=-P_{3,r}>0$, initially increases towards the bottom of the dn^2-potential well and then decreases in time interval $\tau\approx[-0.33K_h+2nK_h,2nK_h]$. The kinetic energy attains its maximal value $K_{e,r,\max}=-P_{3,r,\min}$ at the bottom of the dn^2-potential well at $r=r_{F,2}$. After reflection by the potential wall at $r=r_{\max}$ when $\tau=\tau_{\max}=2nK_h$ and $K_{e,r}=-P_{3,r}=0$, r again primarily accelerates and sequentially decelerates towards the potential barrier for $\tau\approx[2nK_h,+0.33K_h+2nK_h]$. While moving along the potential barrier, r decelerates since $K_{e,r}\approx 0$ for $\tau\approx[0.33K_h+2nK_h,1.66K_h+2nK_h]$. The periodic 3-d trajectory ends at $r=r_{\min}$ when $\tau=\tau_{\min}=+K_h+2nK_h$. The 3-d Hamiltonian map in **Figure 6(d)** qualitatively coincides with that in **Figure 5(d)** since $\mathrm{dn}^2(\tau,\varepsilon_h)=\mathrm{cn}^2(\tau,\varepsilon_h)$ with a graph accuracy. The considered features of the 3-d Hamiltonian map are obviously manifested in the animated **Figure 6(d)**.

4. An Oscillatory Random Model

4.1. The *l*th Mode of the Random Oscillatory cn-Noise

Similarly to the second Hamiltonian system g, we construct the lth mode g_l of the random oscillatory cn-noise in the following form:

$$g_l=A_l\mathrm{cn}(\upsilon_l\tau-K(\varepsilon),\varepsilon), \tag{115}$$

where A_l is an amplitude, υ_l is a frequency of the lth mode, and $l=1,2,\cdots,L$.

Periodic zeroes of g_l

$$g_{l,z}=g_l(\tau_{g,z},\varepsilon)=0 \tag{116}$$

are located at

$$\tau_{g,z}=\frac{2nK(\varepsilon)}{\upsilon_l}, \tag{117}$$

where $n=0,\pm1,\pm2,\cdots$ is an integer.

The lth mode g_l reaches its maximal value

$$g_{l,\max}=g_l(\tau_{g,\max},\varepsilon)=+A_l \tag{118}$$

periodically at

$$\tau_{g,\max}=\frac{(4n+1)K(\varepsilon)}{\upsilon_l} \tag{119}$$

and attains its minimal value

$$g_{l,\min}=g_l(\tau_{g,\min},\varepsilon)=-A_l \tag{120}$$

also periodically at

$$\tau_{g,\min} = \frac{(4n+3)K(\varepsilon)}{\upsilon_l} \tag{121}$$

since the period of oscillation g_l

$$P_{o,l} = \frac{4K(\varepsilon)}{\upsilon_l}. \tag{122}$$

Therefore, range of $g_l \in [g_{l,\min}, g_{l,\max}] = [-A_l, +A_l]$.

Calculating the half of the first derivative of g_l squared and using the independent algebraic relations, we derive the Hamiltonian ODE

$$K_{e,g,l} + P_{4,g,l} = E_{4,g,l} = 0, \tag{123}$$

where $K_{e,g,l}$ is the kinetic energy of g_l,

$$P_{4,g,l} = \frac{\upsilon_l^2}{2A_l^2}(g_l - A_l)(g_l + A_l)(\varepsilon^2 g_l^2 + \delta^2 A_l^2) = \sigma_{4,g,l} g_l^4 + \sigma_{2,g,l} g_l^2 + \sigma_{0,g,l} \tag{124}$$

is an even polynomial potential of the fourth order in g_l with polynomial coefficients

$$[\sigma_{4,g,l}, \sigma_{2,g,l}, \sigma_{0,g,l}] = \left[\frac{\varepsilon^2\upsilon_l^2}{2A_l^2}, \frac{(\delta^2 - \varepsilon^2)\upsilon_l^2}{2}, -\frac{A_l^2\delta^2\upsilon_l^2}{2}\right] \tag{125}$$

and total energy $E_{4,g,l} = 0$. Compared with the polynomial coefficients of g, $\sigma_{4,g,l}$ is inversely proportional to A_l^2, $\sigma_{2,g,l}$ does not depend on A_l^2, $\sigma_{0,g,l}$ is directly proportional to A_l^2, and all coefficients are proportional to υ_l^2.

The lth mode g_l of the random oscillatory cn-noise is a unique solution of the Hamiltonian ODE subjected to the initial conditions

$$g_l\big|_{\tau=0} = 0, \ \frac{\mathrm{d}g_l}{\mathrm{d}\tau}\bigg|_{\tau=0} = 0. \tag{126}$$

In **Figure 7(a)**, g_l is shown for $\upsilon_l = 1$, $\varepsilon = 0.9999$, $K(\varepsilon) = 5.6451$, and various values of A_l: a green dashed curve corresponds to $A_l = 1/2$, a black dotted curve to $A_l = 1$, and a blue solid curve to $A_l = 2$. The value of g_l is directly proportional to amplitude A_l and the initial value of g_l vanishes in accordance with the initial conditions. All curves in **Figure 7** are displayed on time domain $\tau \in [0, 4K(\varepsilon)/\upsilon_l]$.

The Hamiltonian system g_l is displayed in **Figure 7(b)** for $A_l = 1$, $\varepsilon = 0.9999$, and different values of υ_l: a green dashed curve for $\upsilon_l = 1/2$, a black dotted curve for $\upsilon_l = 1$, and a blue solid curve for $\upsilon_l = 2$. Indeed, period $P_{o,l}$ is inversely proportional to υ_l and $P_{o,l} \to +\infty$ as $\upsilon_l \to 0_+$.

The effect of ε on the period and the shape of g_l is visualized in **Figure 7(c)** for $A_l = 1$, $\upsilon_l = 1$, and various values of ε: a green dashed curve for $\varepsilon = \varepsilon_c$ with $K(\varepsilon) = K_c$, a black dotted curve for $\varepsilon = 0.9999$, and a blue solid curve for $\varepsilon = \varepsilon_h$ with $K(\varepsilon) = K_h$. As $\varepsilon \to 1_-$, $P_{o,l} \to +\infty$ and the shape of g_l approaches a sequence of positive and negative pulses $A_l \operatorname{sech}(\upsilon_l \tau)$ with truncated tails because of the vertical asymptote of $K(\varepsilon)$ at $\varepsilon = 1$ [8].

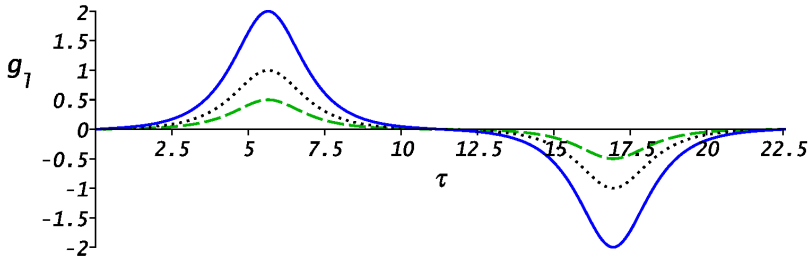

(a)

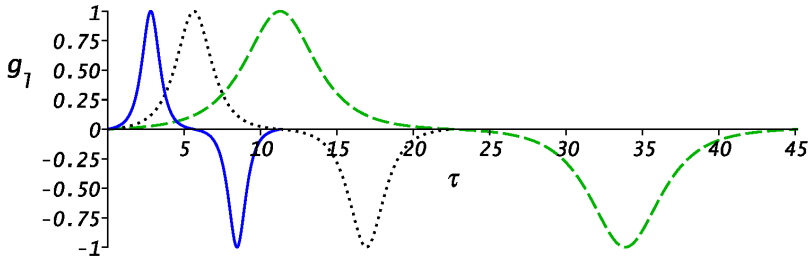

(b)

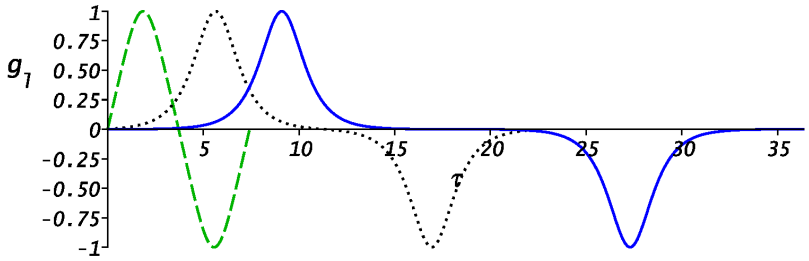

(c)

Figure 7. Plots of the lth mode g_l of the random oscillatory cn-noise for various parameters given in the text.

4.2. The Random Oscillatory cn-Noise with L modes

The random oscillatory cn-noise

$$g_o = \sum_{l=1}^{L} g_l = \sum_{l=1}^{L} A_l \mathrm{cn}\left(\upsilon_l \tau - K(\varepsilon), \varepsilon\right) \tag{127}$$

is a superposition of L modes g_l, where A_l is a random amplitude on interval $[0,1]$.

We then explore an effect of L on the rate of stochastization of the random oscillatory cn-noise for two sequences of frequencies: the Fourier sequence [4] and the Bernoulli sequence [5]. Random oscillatory cn-noise $g_{o,F}$ with the Fourier frequencies and period of the random oscillatory cn-noise $P_{o,F} = 4K(\varepsilon) = 22.5806$ with $\varepsilon = 0.9999$ is shown on interval $\tau \in [0, P_{o,F}]$ in **Figure 8(a)**, **Figure 8(b)**, **Figure 8(c)** for the following five random amplitudes:

$$A_l = [0.388841, 0.854563, 0.425320, 0.573515, 0.777952] \tag{128}$$

and $L = 3,4,5$, respectively.

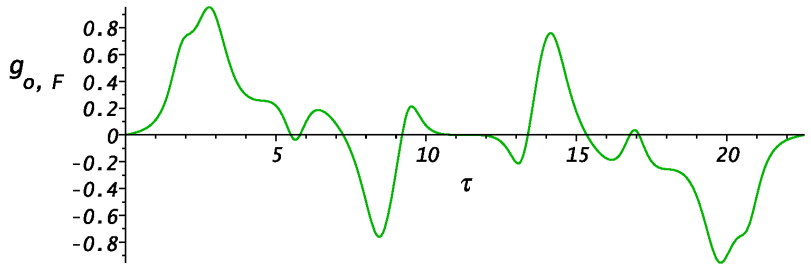

(a)

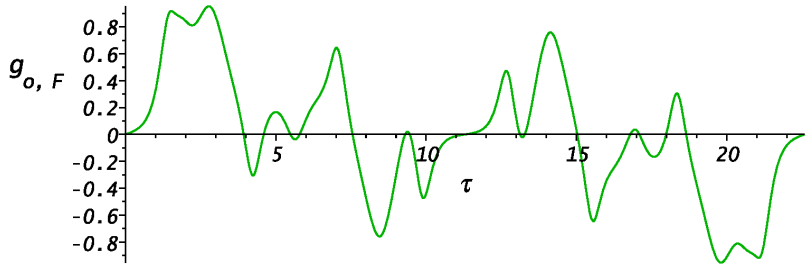

(b)

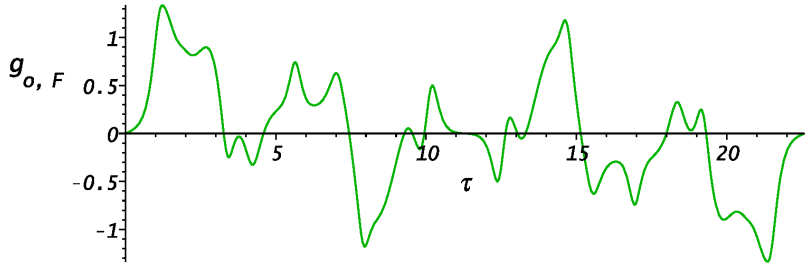

(c)

Figure 8. Plots of the random oscillatory cn-noise for the Fourier frequencies and various L: (a)— $L=3$, (b)— $L=4$, (c)— $L=5$.

Period $P_{o,l,F}$ of the lth mode $g_{l,F}$ has the following values:

$$P_{o,l,F}=\left[22.5806,11.2903,7.52686,5.64515,4.51612\right]. \tag{129}$$

So, numbers $n_{o,l,F}$ of periods $P_{o,l,F}$ in $P_{o,F}$ grow as the Fourier frequencies $\upsilon_{l,F}$, *i.e.* $\upsilon_{l,F}=n_{o,l,F}=P_{o,F}/P_{o,l,F}=\left[1,2,3,4,5\right]$. The rate of stochastization of $g_{o,F}$ is a lowest one since $P_{o,F}$ does not depend on L and stochastization of the random oscillatory cn-noise is caused only by growth of number of amplitudes and frequencies with L.

However, simplicity of curves in **Figures 8(a)-(c)** clearly demonstrates an odd symmetry of g_o for all sequences of frequencies. Interval $\left[0,P_o\right]$ contains integer number $n_{o,l}$ of subintervals $\left[0,P_{o,l}\right]$ for g_l, *i.e.*

$$P_o=n_{o,l}P_{o,l}. \tag{130}$$

All g_l vanish at the end points of subintervals $\left[0,P_{o,l}\right]$. Therefore, g_o vanishes at the end points of interval $\left[0,P_o\right]$, namely,

$$g_o\left(0,\varepsilon\right)=0,\ g_o\left(P_o,\varepsilon\right)=0. \tag{131}$$

If $n_{o,l}$ is even, then the midpoint of $[0,P_o]$ becomes an endpoint of $[0,P_{o,l}]$, where g_l vanishes, *viz.*

$$P_o = 2kP_{o,l},\ \frac{P_o}{2} = kP_{o,l},\ g_{o,l}\left(\frac{P_o}{2},\varepsilon\right) = 0. \tag{132}$$

If $n_{o,l}$ is odd, then the midpoint of $[0,P_o]$ becomes a midpoint of $[0,P_{o,l}]$. Then g_l vanishes at the midpoint of subinterval $[0,P_{o,l}]$, as well, *i.e.*

$$P_o = (2k+1)P_{o,l},\ \frac{P_o}{2} = \left(k+\frac{1}{2}\right)P_{o,l},\ g_{o,l}\left(\frac{P_o}{2},\varepsilon\right) = 0. \tag{133}$$

So, g_o vanishes at the midpoint of $[0,P_o]$ as the sum of g_l vanishing both for even and odd $n_{o,l}$, namely,

$$g_o\left(\frac{P_o}{2},\varepsilon\right) = 0. \tag{134}$$

Since an odd symmetry

$$g_l(\tau-\tau_{g,z},\varepsilon) = -g_l(-(\tau-\tau_{g,z}),\varepsilon) \tag{135}$$

holds for all periodic zeroes of g_l (see **Figures 7(a)-(c)**), the odd symmetry is valid at the midpoint and endpoints for all g_l and, therefore, the odd symmetry is also valid at the midpoint of $[0,P_o]$ for g_o:

$$g_o\left(\tau-\frac{P_o}{2},\varepsilon\right) = -g_o\left(-\left(\tau-\frac{P_o}{2}\right),\varepsilon\right). \tag{136}$$

Vanishing of g_o at the end points and the midpoint of $[0,P_o]$ and the odd symmetry of g_o with respect to the midpoint of $[0,P_o]$ is illustrated for various L and υ_l in **Figures 8(a)-(c)** and **Figures 9(a)-(b)**.

Random oscillatory cn-noise $g_{o,B}$ with $\varepsilon = 0.9999$, the Bernoulli frequencies $\upsilon_{l,B} = [1,1/2,1/3,1/5,1/7]$, the same random amplitudes A_l, and periods of the random oscillatory cn-noise $P_{o,B} = 135.484, 677.418, 4741.92$ is visualized on interval $\tau \in [0,P_{o,B}]$ in **Figure 9(a)**, **Figure 9(b)**, **Figure 9(c)** for $L = 3,4,5$, respectively.

Periods $P_{o,l,B} = 4K(\varepsilon)/\upsilon_{l,B}$ of the lth mode $g_{l,B}$ increase, *viz.*

$$P_{o,l,B} = [22.5806, 45.1612, 67.7418, 112.903, 158.064], \tag{137}$$

where

$$P_{o,B} = LCM\left(P_{o,1,B},\cdots,P_{o,l,B},\cdots,P_{o,L,B}\right) \tag{138}$$

and *LCM* stands for the least common multiple.

For $L = 5$, numbers $n_{o,l,B}$ of periods $P_{o,l,B}$ in $P_{o,B}$ decrease as follows: $n_{o,l,B} = P_{o,B}/P_{o,l,B} = [210,105,70,42,30]$. The rate of stochastization of $g_{o,B}$ has a highest value since $P_{o,B}$ grows as a product of prime numbers. For $L = 3$, $P_{o,B}$ is greater six times than the period of the first mode $P_{o,1,B}$. For $L = 4$, $P_{o,B}$ is larger 30 times, and, for $L = 5$, $P_{o,B}$ exceeds $P_{o,1,B}$ 210 times. To summarize, $g_{o,B}$ emulates a smooth random oscillatory variable with an unbounded period at high values of L since $P_{o,B} \to \infty$ as $L \to \infty$.

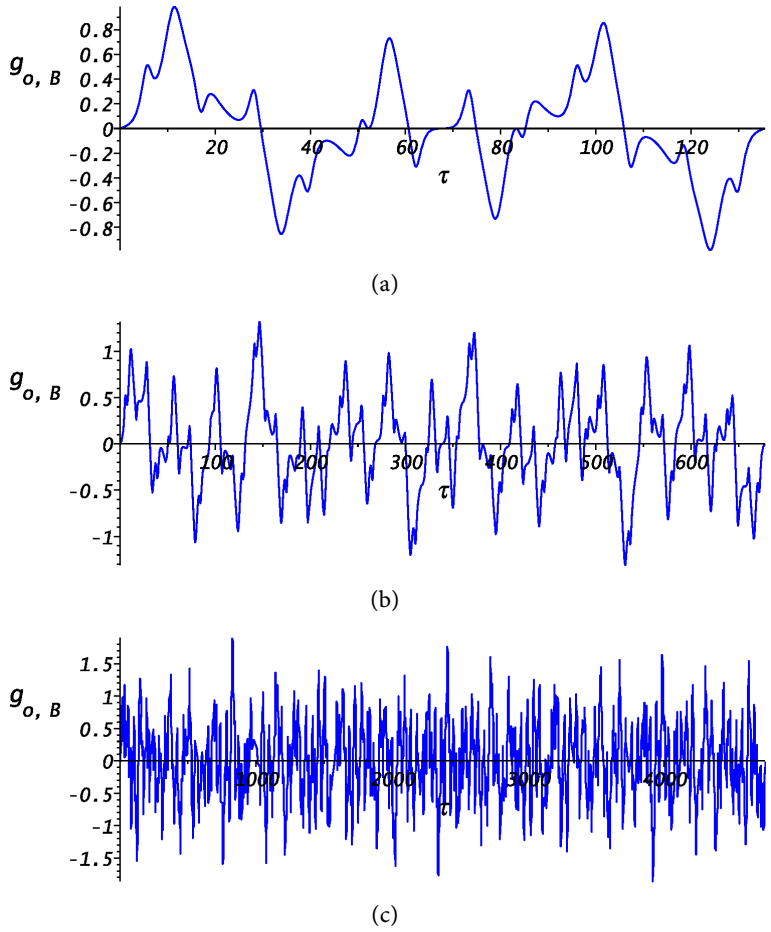

Figure 9. Plots of the random oscillatory cn-noise for the Bernoulli frequencies and various L: (a)— $L=3$, (b)— $L=4$, (c)— $L=5$.

The rates of stochastization of the random oscillatory cn-noise with the Fourier and Bernoulli frequencies are compared in **Figure 10**, where $\ln\left(P_{o,F}\right)$ versus L is shown by green circles and a dotted black line and $\ln\left(P_{o,B}\right)$ by blue diamonds and a dashed black line. For $L\geq 4$, $P_{o,B}$ grows exponentially as follows:

$$\ln\left(P_{o,B}\right)=-4.2408+2.6552L,\ P_{o,B}=0.0014397\exp\left(2.6552L\right), \tag{139}$$

where coefficients are computed by minimizing the least-squares error.

We then compare histogram of g_o for the Fourier and Bernoulli frequencies with the density of the Gaussian (normal) probability distribution

$$p_o=\frac{1}{\sqrt{2\pi}\,\sigma_o}\exp\left(-\frac{\left(g_o-\mu_o\right)^2}{2\sigma_o^2}\right), \tag{140}$$

where μ_o is the mean and σ_o^2 is the variance of discrete data sample $g_{o,k}$ of size K_o, which are computed by the formulas of the descriptive statistics [9]:

$$\mu_o=\frac{\sum_{k=1}^{K_o}g_{o,k}}{K_o},\ \sigma_o^2=\frac{\sum_{k=1}^{K_o}\left(g_{o,k}-\mu_o\right)^2}{K_o-1},\ g_{o,k}=g_o\left(\tau_k\right). \tag{141}$$

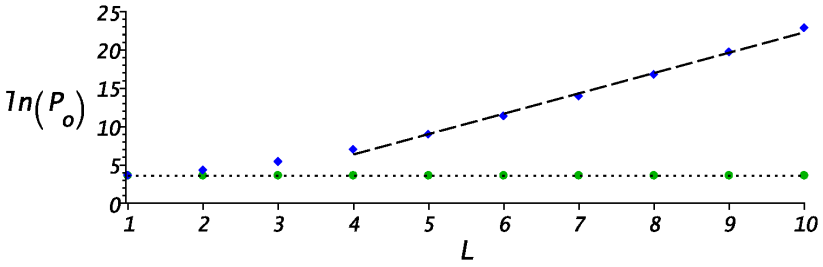

Figure 10. Plots of $\ln(P_o)$ versus L of the random oscillatory cn-noise.

Here, moments of time τ_k as selected as equidistant points on interval $\tau \in [0, P_o]$, where P_o is the period of the random oscillatory cn-noise.

Histograms in **Figure 11(a)** and **Figure 11(b)** are computed with random amplitudes A_l, $\varepsilon = 0.9999$, and $L = 5$ for the Fourier and Bernoulli frequencies, respectively. The data sample sizes $K_{o,F} = 416$ and $K_{o,B} = 3840$ are equal to the number of computational points of plots $g_{o,F}$ and $g_{o,B}$ in **Figure 8(c)** and **Figure 9(c)**, correspondingly.

In **Figure 11**, $\mu_{o,F} = 0, \mu_{o,B} = 0$ and $\sigma_{o,F} = 0.580233, \sigma_{o,F} = 0.537277$, whereas the Gaussian probability distribution is displayed by a solid orange line. As L increases, $p_{o,F}$ develops into the normal distribution. However, even for $L = 5$, the tails of the normal distribution are not reproduced and noticeable deviations from the Gaussian distribution still remain. As L grows, $p_{o,B}$ approaches the Gaussian distribution much faster. For $L \geq 5$, the normal distribution is reproduced with graph accuracy.

5. A Pulsatory Random Model

5.1. The *l*th Mode of the Random Pulsatory cn²-Noise

Analogously to the second Hamiltonian system squared q, we define the lth mode q_l of the random pulsatory cn²-noise as follows:

$$q_l = A_l \mathrm{cn}^2\left(\upsilon_l \tau - K(\varepsilon), \varepsilon\right), \tag{142}$$

where A_l is an amplitude and υ_l is a frequency of the lth mode, and $l = 1, 2, \cdots, L$.

Periodic minimums of q_l, which are periodic zeroes of q_l,

$$q_{l,\min} = q_l\left(\tau_{q,\min}, \varepsilon\right) = 0 \tag{143}$$

are positioned at

$$\tau_{q,\min} = \frac{2nK(\varepsilon)}{\upsilon_l}, \tag{144}$$

where $n = 0, \pm 1, \pm 2, \cdots$ is an integer.

The lth mode q_l attains its maximal value

$$q_{l,\max} = q_l\left(\tau_{q,\max}, \varepsilon\right) = A_l \tag{145}$$

periodically at

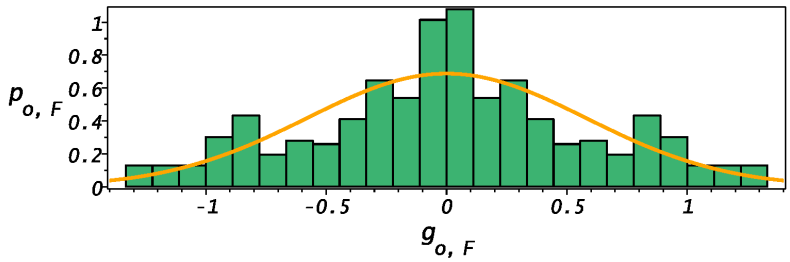

(a)

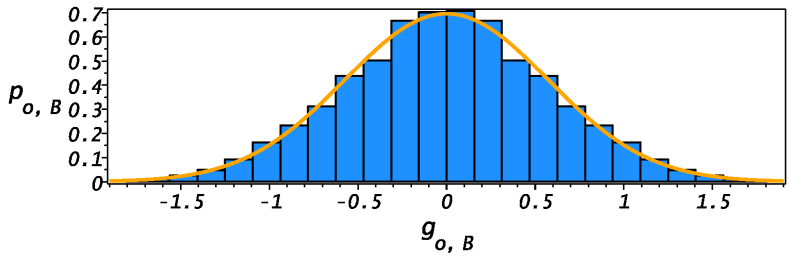

(b)

Figure 11. Histogram of the random oscillatory cn-noise: (a)—for the Fourier frequencies, (b)—for the Bernoulli frequencies.

$$\tau_{q,\max} = \frac{(2n+1)K(\varepsilon)}{\upsilon_l}, \tag{146}$$

because the period of pulsation q_l

$$P_{p,l} = \frac{2K(\varepsilon)}{\upsilon_l}. \tag{147}$$

Consequently, range of $q_l \in \left[q_{l,\min}, q_{l,\max}\right] = \left[0, A_l\right]$.

Computation of the half of the first derivative of q_l squared and application of the independent algebraic relations yield the Hamiltonian ODE

$$K_{e,q,l} + P_{3,q,l} = E_{3,q,l} = 0, \tag{148}$$

where $K_{e,q,l}$ is the kinetic energy of the Hamiltonian system q_l,

$$P_{3,q,l} = \frac{2\upsilon_l^2}{A_l}\left(q_l - A_l\right)q_l\left(\varepsilon^2 q_l + \delta^2 A_l\right) = \sigma_{3,q,l}q_l^3 + \sigma_{2,q,l}q_l^2 + \sigma_{1,q,l}q_l \tag{149}$$

is a polynomial potential of the third order in q_l with polynomial coefficients

$$\left[\sigma_{3,q,l}, \sigma_{2,q,l}, \sigma_{1,q,l}\right] = \left[\frac{2\varepsilon^2\upsilon_l^2}{A_l}, 2\left(\delta^2 - \varepsilon^2\right)\upsilon_l^2, -2\delta^2 A_l\,\upsilon_l^2\right] \tag{150}$$

and total energy $E_{3,q,l} = 0$. Compared with the polynomial coefficients of q, $\sigma_{3,q,l}$ is inversely proportional to A_l, $\sigma_{2,q,l}$ does not depend on A_l, $\sigma_{1,q,l}$ is directly proportional to A_l, and all coefficients are proportional to υ_l^2.

The lth mode q_l of the pulsatory cn^2-noise represents a unique solution of the Hamiltonian ODE with the following initial conditions:

$$q_l\big|_{\tau=0} = 0, \ \left.\frac{\mathrm{d}q_l}{\mathrm{d}\tau}\right|_{\tau=0} = 0. \tag{151}$$

In Figure 12(a), q_l is displayed for $\upsilon_l = 1$, $\varepsilon = 0.9999$, $K(\varepsilon) = 5.6451$, and different values of A_l: a green dashed curve corresponds to $A_l = 1/2$, a black dotted curve to $A_l = 1$, and a blue solid curve to $A_l = 2$. The value of q_l is directly proportional to amplitude A_l and the initial value of q_l vanishes in agreement with the initial conditions. Pulsations q_l are sharper than pulsations g_l in the same manner as pulsations $A_l \operatorname{sech}^2(\upsilon_l \tau)$ are sharper than pulsations $A_l \operatorname{sech}(\upsilon_l \tau)$. All curves in Figure 12 are visualized on time domain $\tau \in [0, 4K(\varepsilon)/\upsilon_l]$.

The Hamiltonian system q_l is visualized in Figure 12(b) for $A_l = 1$, $\varepsilon = 0.9999$, and various values of υ_l: a green dashed curve for $\upsilon_l = 1/2$, a black dotted curve for $\upsilon_l = 1$, and a blue solid curve for $\upsilon_l = 2$. In the view of the definition, period $P_{p,l}$ is inversely proportional to υ_l and $P_{p,l} \to +\infty$ as $\upsilon_l \to 0_+$.

The effect of ε on the period and the shape of q_l is represented in Figure 12(c) for $A_l = 1$, $\upsilon_l = 1$, and various values of ε: a green dashed curve for $\varepsilon = \varepsilon_c$, a black dotted curve for $\varepsilon = 0.9999$, and a blue solid curve for $\varepsilon = \varepsilon_h$. As $\varepsilon \to 1_-$, $P_{p,l} \to +\infty$ and the shape of q_l tends to a sequence of pulses $A_l \operatorname{sech}^2(\upsilon_l \tau)$ with truncated tails.

5.2. The Random Pulsatory cn²-Noise with *L* Modes

The random pulsatory cn²-noise

$$q_p = \sum_{l=1}^{L} q_l = \sum_{l=1}^{L} A_l \operatorname{cn}^2(\upsilon_l \tau - K(\varepsilon), \varepsilon) \tag{152}$$

is a superposition of L modes q_l, where A_l is the random amplitude on interval $[0,1]$.

The random pulsatory cn²-noise $q_{p,F}$ with the Fourier frequencies $\upsilon_{l,F} = [1,2,3,4,5]$, $\varepsilon = 0.999866$, a period of the pulsatory noise $P_{p,F} = 2K(\varepsilon) = 10.9978$, and random amplitudes A_l is displayed on interval $\tau \in [0, P_{p,F}]$ in Figure 13(a), Figure 13(b), Figure 13(c) for $L = 3,4,5$, correspondingly.

Period $P_{p,l,F}$ of the lth mode $q_{l,F}$ contains the following values:

$$P_{p,l,F} = [10.9978, 5.49889, 3.66593, 2.74945, 2.19956]. \tag{153}$$

Therefore, numbers $n_{p,l,F}$ of periods $P_{p,l,F}$ in $P_{p,F}$ also increase as the Fourier frequencies $\upsilon_{l,F}$, *viz.* $n_{p,l,F} = P_{p,F}/P_{p,l,F} = [1,2,3,4,5]$. The rate of stochastization of $q_{p,F}$ has a lowest value because $P_{p,F}$ does not depend on L and stochastization of the random pulsatory cn²-noise is induced by increase in number of amplitudes and frequencies with L.

Curves in Figures 13(a)-(c) obviously display an even symmetry of q_p for all sequences of frequencies. Interval $[0, P_p]$ includes integer number $n_{p,l}$ of subintervals $[0, P_{p,l}]$ for q_l, namely,

$$P_p = n_{p,l} P_{p,l}. \tag{154}$$

All q_l vanish at the end points of subintervals $\left[0, P_{p,l}\right]$. So, q_p also vanishes at the end points of interval $\left[0, P_p\right]$, *viz.*

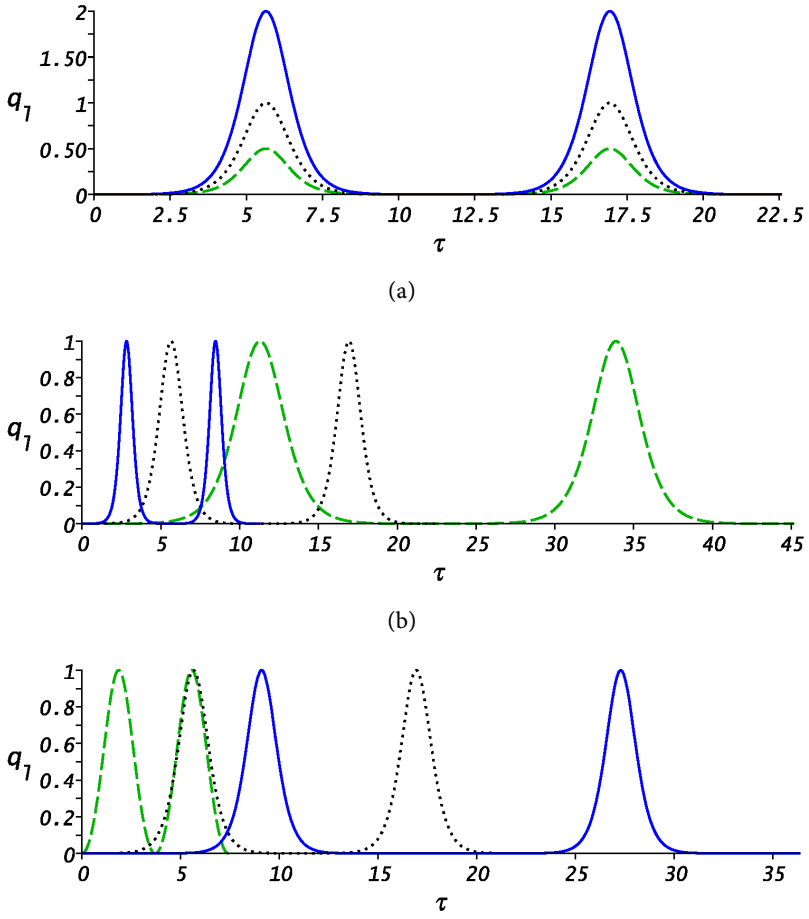

Figure 12. Plots of the lth mode q_l of the random oscillatory cn^2-noise for various parameters given in the text.

$$q_p\left(0,\varepsilon\right)=0,\ q_p\left(P_p,\varepsilon\right)=0. \tag{155}$$

If $n_{p,l}$ is even, then the midpoint of $\left[0, P_p\right]$ becomes an endpoint of $\left[0, P_{p,l}\right]$, where q_l vanishes, *i.e.*

$$P_p=2kP_{p,l},\ \frac{P_p}{2}=kP_{p,l},\ q_{p,l}\left(\frac{P_p}{2},\varepsilon\right)=0. \tag{156}$$

If $n_{p,l}$ is odd, then the midpoint of $\left[0, P_p\right]$ becomes a midpoint of $\left[0, P_{p,l}\right]$. Then q_l reaches local maximum A_l at the midpoint of subinterval $\left[0, P_{p,l}\right]$, *viz.*

$$P_p=\left(2k+1\right)P_{p,l},\ \frac{P_p}{2}=\left(k+\frac{1}{2}\right)P_{p,l},\ q_{p,l}\left(\frac{P_p}{2},\varepsilon\right)=A_l. \tag{157}$$

Thus, q_p attains a local maximum at the midpoint of $\left[0, P_p\right]$ as the sum of

$q_l = 0$ for even $n_{p,l}$ and $q_l = A_l$ for odd $n_{p,l}$, explicitly,

$$q_p\left(\frac{P_p}{2}, \varepsilon\right) = q_{p,\max}. \tag{158}$$

Because an even symmetry

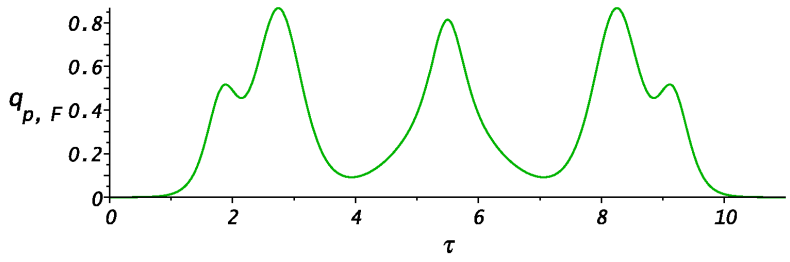

(a)

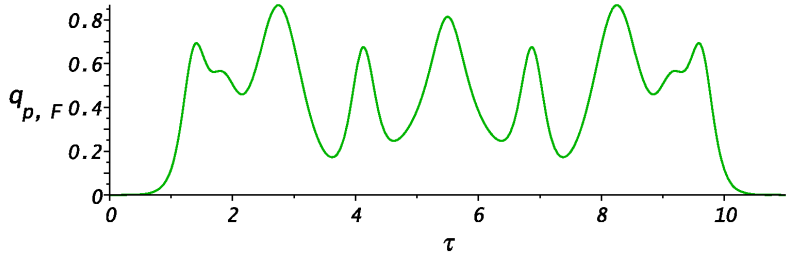

(b)

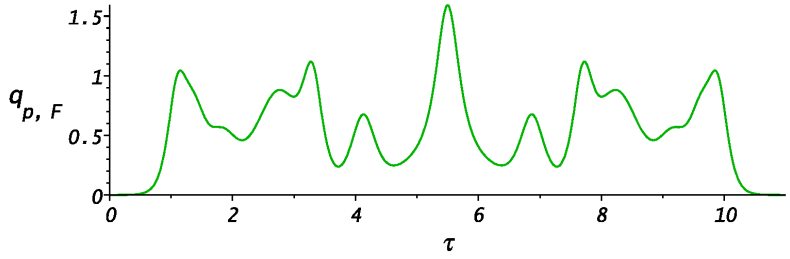

(c)

Figure 13. Plots of the random pulsatory cn^2-noise for the Fourier frequencies and various L: (a)— $L = 3$, (b)— $L = 4$, (c)— $L = 5$.

$$\begin{aligned} q_l\left(\tau - \tau_{q,\min}, \varepsilon\right) &= q_l\left(-\left(\tau - \tau_{q,\min}\right), \varepsilon\right), \\ q_l\left(\tau - \tau_{q,\max}, \varepsilon\right) &= q_l\left(-\left(\tau - \tau_{q,\max}\right), \varepsilon\right) \end{aligned} \tag{159}$$

is valid for all periodic zeroes (minimums) and periodic maximums of q_l (see Figures 12(a)-(c)), the even symmetry also holds for the midpoint of $\left[0, P_p\right]$ for all q_l and, consequently, for q_p:

$$q_p\left(\tau - \frac{P_p}{2}, \varepsilon\right) = q_p\left(-\left(\tau - \frac{P_p}{2}\right), \varepsilon\right). \tag{160}$$

Vanishing of q_p at the end points of interval $\left[0, P_p\right]$ and the even symmetry of q_p with respect to the midpoint of $\left[0, P_p\right]$ are visualized for various L

and υ_l in Figures 13(a)-(c), Figures 14(a)-(b). We also observe that periodic zeroes of q_l frequently do not become zeroes of q_p since zeroes of q_l happen at the various times for different l.

Random pulsatory cn²-noise $q_{p,B}$ with the Bernoulli frequencies $\upsilon_{l,B}=[1,1/2,1/3,1/5,1/7]$, the same random amplitudes A_l, $\varepsilon=0.999866$, and periods of the random pulsatory cn²-noise $P_{p,B}=65.9867,329.933,2309.53$ is shown on interval $\tau\in[0,P_{p,B}]$ in Figure 14(a), Figure 14(b), and Figure 14(c) for $L=3,4,5$, respectively.

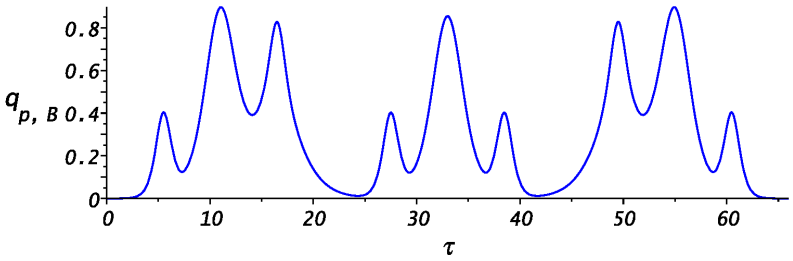

(a)

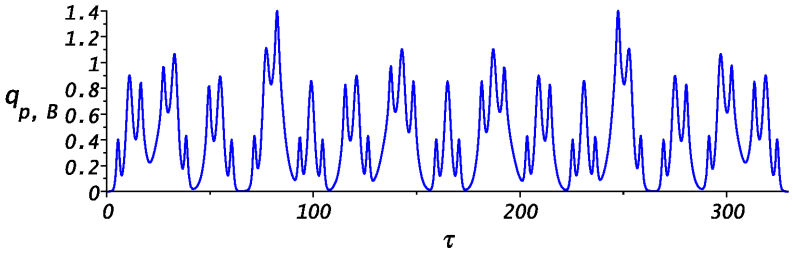

(b)

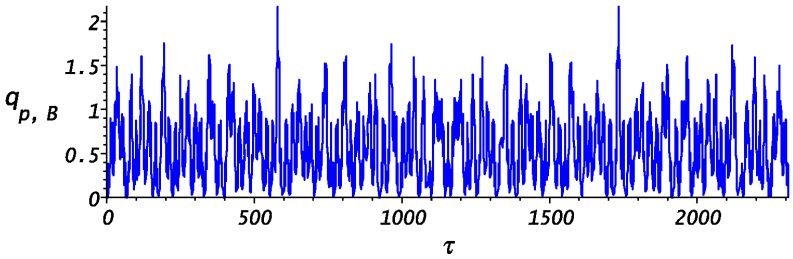

(c)

Figure 14. Plots of the random pulsatory cn²-noise for the Bernoulli frequencies and various L: (a)— $L=3$, (b)— $L=4$, (c)— $L=5$.

Periods $P_{p,l,B}=2K(\varepsilon)/\upsilon_{l,B}$ of the lth mode $q_{l,B}$ represent the following increasing sequence:

$$P_{p,l,B}=[10.9978,21.9956,32.9933,54.9889,76.9845], \tag{161}$$

where

$$P_{p,B}=LCM\left(P_{p,1,B},\cdots,P_{p,l,B},\cdots,P_{p,L,B}\right). \tag{162}$$

For $L=5$, numbers $n_{p,l,B}$ of periods $P_{p,l,B}$ in $P_{p,B}$ decrease the same way

as for the random oscillatory cn-noise: $n_{p,l,B} = P_{p,B}/P_{p,l,B} = [210,105,70,42,30]$. The rate of stochastization of $q_{p,B}$ has a maximal value since $P_{p,B}$ increases as a product of prime numbers. Therefore, for $L=3$, $P_{p,B}$ is six times larger than the period of the first mode $P_{p,1,B}$. For $L=4$, $P_{p,B}$ is 30 times greater, and, for $L=5$, $P_{p,B}$ is 210 times larger than $P_{p,1,B}$. To summarize, $q_{p,B}$ models a smooth random pulsatory variable with an unbounded period at large values of L because $P_{o,B} \to \infty$ as $L \to \infty$.

We compare the rates of stochastization of the random pulsatory cn^2-noise for the Fourier and Bernoulli frequencies in Figure 15, where $\ln(P_{p,F})$ versus L is displayed by green circles and a dotted black line and $\ln(P_{p,B})$ by blue diamonds and a dashed black line. For $L \geq 4$, the period of the pulsatory cn^2-noise $P_{p,B}$ with the Bernoulli frequencies increases exponentially since

$$\ln(P_{p,B}) = -4.9339 + 2.6552L, \ P_{o,B} = 0.0071983\exp(2.6552L), \tag{163}$$

where coefficients are obtained by the least-squares fit.

Density $p_o(g_o)$ of the Gaussian probability distribution with mean μ_o, variance σ_o^2, and normalization coefficient c_o for random oscillatory variable g_o, which may take both positive and negative values as $-\infty < g_o < +\infty$,

$$p_o(g_o) = \frac{c_o}{\sigma_o}\exp\left(-\frac{(g_o-\mu_o)^2}{2\sigma_o^2}\right), \ c_o = \frac{1}{\sqrt{2\pi}} \tag{164}$$

satisfies the following normalization condition:

$$\int_{-\infty}^{+\infty} p_o(g_o)\mathrm{d}g_o = 1. \tag{165}$$

Consider density $p_p(q_p)$ of the truncated Gaussian probability distribution [9] with mean μ_p, variance σ_p^2, and normalization coefficient c_p for random pulsatory variable q_p, which may take only positive values since $0 \leq q_p < +\infty$,

$$p_p(q_p) = \frac{c_p}{\sigma_p}\exp\left(-\frac{(q_p-\mu_p)^2}{2\sigma_p^2}\right). \tag{166}$$

This density satisfies the correspondent normalization condition

$$\int_{0}^{+\infty} p_p(q_p)\mathrm{d}q_p = 1. \tag{167}$$

To find the normalization coefficient of $p_p(q_p)$, we decompose the normalization integral into two parts

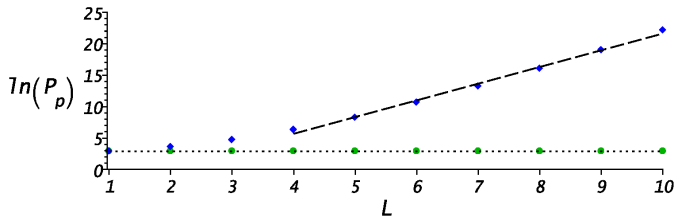

Figure 15. Plots of $\ln(P_p)$ versus L of the random pulsatory cn^2-noise.

$$\int_0^{+\infty} p_p\left(q_p\right)\mathrm{d}q_p = \int_0^{\mu_p} p_p\left(q_p\right)\mathrm{d}q_p + \int_{\mu_p}^{+\infty} p_p\left(q_p\right)\mathrm{d}q_p \tag{168}$$

and take the integrals separately

$$\int_0^{\mu_p} p_p\left(q_p\right)\mathrm{d}q_p = c_p\sqrt{\frac{\pi}{2}}\mathrm{erf}\left(\frac{\mu_p}{\sqrt{2}\,\sigma_p}\right),\quad \int_{\mu_p}^{+\infty} p_p\left(q_p\right)\mathrm{d}q_p = c_p\sqrt{\frac{\pi}{2}}. \tag{169}$$

Thus, an algebraic form of the normalization condition becomes

$$c_p\sqrt{\frac{\pi}{2}}\left[1+\mathrm{erf}\left(\frac{\mu_p}{\sqrt{2}\,\sigma_p}\right)\right]=1. \tag{170}$$

Solving it with respect to c_p and back-substituting yield

$$p_p\left(q_p\right)=\frac{\sqrt{\frac{2}{\pi}}\exp\left(-\frac{\left(q_p-\mu_p\right)^2}{2\sigma_p^2}\right)}{\sigma_p\left[1+\mathrm{erf}\left(\frac{\mu_p}{\sqrt{2}\,\sigma_p}\right)\right]}, \tag{171}$$

where the error function

$$\mathrm{erf}\left(w\right)=\frac{2}{\sqrt{\pi}}\int_0^w \exp\left(-u^2\right)\mathrm{d}u. \tag{172}$$

Density $p_p\left(q_p\right)$ of the truncated Gaussian probability distribution is shown by a solid blue curve and density $p_o\left(q_p\right)$ of the Gaussian probability distribution is displayed by a dotted blue curve in Figure 16(a), Figure 16(a), Figure 16(c) for $\sigma_p^2=1$ and $\mu_p=-1/2,0,+1/2$, respectively. A common area beneath $p_p\left(q_p\right)$ and $p_o\left(q_p\right)$ is shadowed by a blue color. A truncated part under $p_o\left(q_p\right)$ is shadowed by a yellow color. Due to the normalization condition, this area is equal to an area between the solid and dotted curves for $q_p\geq 0$, which is also visualized by yellow.

Figure 16(a) demonstrates that $p_p\left(q_p\right)$ looks like the tail of a rescaled normal probability distribution for negative μ_p. For $\mu_p=0$ in Figure 16(b), the area between $p_p\left(q_p\right)$ and the x-axis exceeds twice the blue shadowed area between $p_o\left(q_p\right)$ and the x-axis since $\mathrm{erf}\left(0\right)=0$ and

$$\lim_{\mu_p\to 0} p_p\left(q_p\right)=2p_o\left(q_p\right). \tag{173}$$

As μ_p becomes positive in Figure 16(c), the yellow shadowed area between $p_p\left(q_p\right)$ and $p_o\left(q_p\right)$ gradually diminishes because $\mathrm{erf}\left(\infty\right)=1$ and

$$\lim_{\mu_p\to\infty} p_p\left(q_p\right)=p_o\left(q_p\right). \tag{174}$$

Histograms in Figure 17(a) and Figure 17(b) are obtained with the same random amplitudes A_l, $\varepsilon=0.999866$, and $L=5$ for the Fourier frequencies and Bernoulli frequencies, correspondingly. The data sample sizes $K_{p,F}=388$ and $K_{p,B}=4649$ are the same as the number of computational points of plots $q_{p,F}$ and $q_{p,B}$ in Figure 13(c) and Figure 14(c), respectively.

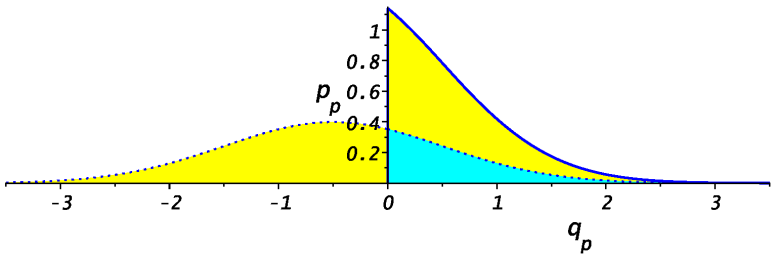

(a)

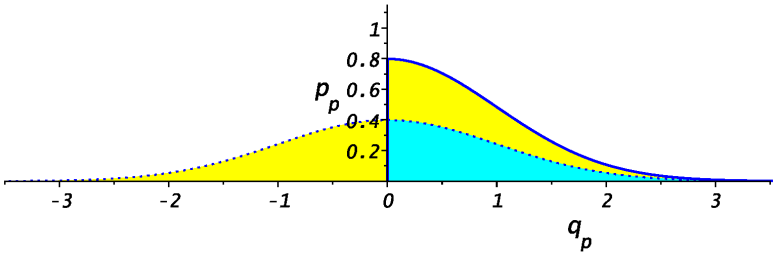

(b)

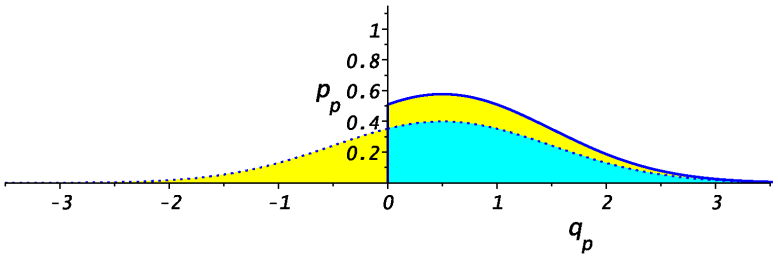

(c)

Figure 16. Plots of the truncated Gaussian probability distribution for $\sigma_p^2 = 1$ and various μ_p: (a)— $\mu_p = -1/2$, (b)— $\mu_p = 0$, (c)— $\mu_p = +1/2$.

In **Figure 17**, $\mu_{p,F} = 0.429347$, $\mu_{p,B} = 0.0007767$ together with $\sigma_{p,F} = 0.461963$, $\sigma_{p,F} = 0.717548$ are computed by the numeric least-squares fit, while the truncated Gaussian probability distribution is shown by a solid orange line. As L grows, $p_{p,F}$ evolves into the truncated normal distribution. Even for $L = 5$, there are obvious deviations from the truncated Gaussian distribution. As L increases, $p_{p,B}$ transforms into the truncated Gaussian distribution much faster. For $L \geq 5$, the truncated normal distribution is emulated with graph accuracy.

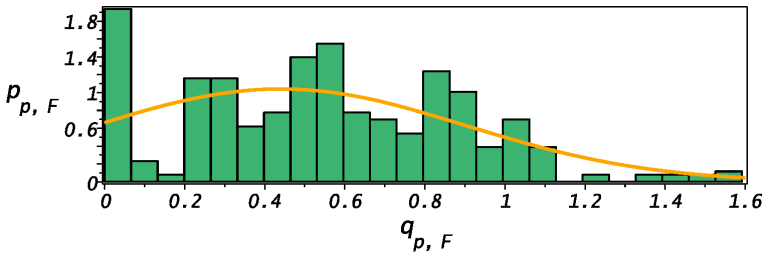

(a)

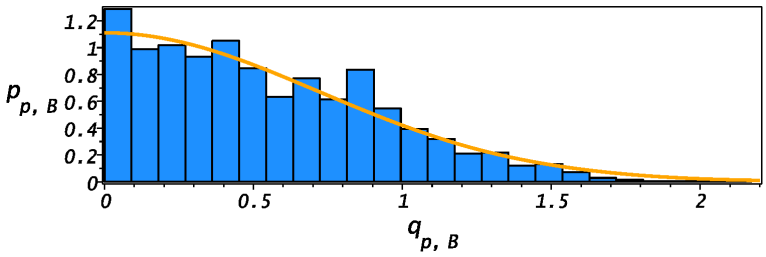

(b)

Figure 17. Histogram of the random oscillatory cn²-noise: (a)—for the Fourier frequencies, (b)—for the Bernoulli frequencies.

6. Conclusions

We have meticulously studied six oscillatory and pulsatory dynamic models of a conservative perturbation with vanishing total energy with the help of the Hamiltonian and Newtonian dynamics of the first triplet of copolar elliptic functions and the first triplet of copolar elliptic functions squared.

As $\varepsilon \to 1_-$, the first Hamiltonian system $f = f(\tau, \varepsilon)$ represents the nonlinear sn-oscillation in range $f \in [-1, +1]$ with period $4K(\varepsilon)$ that displays a sequence of positive and negative rectangular pulses of the tanh-shape in $f \in [0, +1]$, $f \in [-1, 0]$ for $\tau \in [4nK(\varepsilon), 2K(\varepsilon) + 4nK(\varepsilon)]$, $\tau \in [2K(\varepsilon) + 4nK(\varepsilon), 4K(\varepsilon) + 4nK(\varepsilon)]$, respectively, where $n = 0, \pm 1, \pm 2, \cdots$. The second Hamiltonian system $g = g(\tau, \varepsilon)$ describes the nonlinear cn-oscillation in range $g \in [-1, +1]$ with period $4K(\varepsilon)$ that manifests a sequence of positive and negative point pulses of the sech-shape in $g \in [0, +1]$, $g \in [-1, 0]$ for $\tau \in [-K(\varepsilon) + 4nK(\varepsilon), +K(\varepsilon) + 4nK(\varepsilon)]$, $\tau \in [K(\varepsilon) + 4nK(\varepsilon), 3K(\varepsilon) + 4nK(\varepsilon)]$, correspondingly. The third Hamiltonian system $h = h(\tau, \varepsilon)$ specifies the nonlinear dn-pulsation with period $2K(\varepsilon)$ that displays a sequence of positive point pulses of the sech-shape in range $h \in [\delta, 1]$ for $\tau \in [-K(\varepsilon) + 2nK(\varepsilon), +K(\varepsilon) + 2nK(\varepsilon)]$.

As $\varepsilon \to 1_-$, the fourth Hamiltonian system $p = p(\tau, \varepsilon)$ presents the nonlinear sn²-pulsation with period $2K(\varepsilon)$ that exhibits a sequence of positive rectangular pulses of the tanh²-shape in range $p \in [0, 1]$ for $\tau \in [2nK(\varepsilon), 2K(\varepsilon) + 2nK(\varepsilon)]$. The fifth Hamiltonian system $q = q(\tau, \varepsilon)$ expresses the nonlinear cn²-pulsation with period $2K(\varepsilon)$ that is visualized by a sequence of positive point pulses of the sech²-shape in range $q \in [0, 1]$ for $\tau \in [-K(\varepsilon) + 2nK(\varepsilon), +K(\varepsilon) + 2nK(\varepsilon)]$. The sixth Hamiltonian system $r = r(\tau, \varepsilon)$ defines the nonlinear dn²-pulsation with period $2K(\varepsilon)$ that is established by a sequence of positive point pulses of the sech²-shape in range $r \in [\delta^2, 1]$ for $\tau \in [-K(\varepsilon) + 2nK(\varepsilon), +K(\varepsilon) + 2nK(\varepsilon)]$.

Using the Hamiltonian systems g and q of conservative perturbations with the vanishing total energy, two stochastic models have been developed. First, the

smooth stochastic model g_o of the random oscillatory cn-noise, which depends on random amplitudes A_l, elliptic modulus ε, frequency sequence υ_l, and number L of modes g_l. Dependence of g_l on parameters $A_l, \varepsilon, \upsilon_l$ have been studied and the odd symmetry of g_o for all sequences of frequencies have been shown. Numerical experiments show that for the Bernoulli frequencies g_o approaches a smooth random oscillatory variable with an unbounded period and the Gaussian probability distribution as an exponential function of L.

Second, the smooth stochastic model q_p of the random pulsatory cn^2-noise, which is determined by $A_l, \varepsilon, \upsilon_l$, and number L of modes q_l. We then explore dependence of q_l on $A_l, \varepsilon, \upsilon_l$ and prove the even symmetry of q_p for all sequences of frequencies. Numerical experiments demonstrate that for the Bernoulli frequencies q_p approaches a smooth random pulsatory variable with an unbounded period and the truncated Gaussian probability distribution as an exponential function of L.

A point-by-point comparison of the stochastic models of the current paper with experimental data is impossible since smooth stochastic functions with an unbounded period are never repeated. Each implementation of the stochastic models produces another version of stochastic data. However, a qualitative comparison with experimental data is presented in the current paper, especially in **Figure 9(c)** and **Figure 14(c)**, where a typical realization of white noise is represented for oscillations and pulsations, respectively. A single quantitative issue, which is used to compare theoretical and experimental stochastic data, is a probability distribution of random variables. This comparison is provided in **Figure 11(b)** and **Figure 17(b)**, where the stochastic data generated by the random models fit with graph accuracy the Gaussian probability distribution and the truncated Gaussian probability distribution for the oscillatory white noise and the pulsatory white noise, correspondingly.

Although the paper was originally aimed at development of exact wave turbulence, its results are applicable in a much broader realm of applications since the stochastic models are constructed independently from the deterministic models. The developed random models describe conservative perturbations with vanishing total energies, which should be initiated once and then need not an external source of energy to maintain them. Another attractive property of elliptic functions is a variable period, which allows the models of the oscillatory white noise and the pulsatory white noise to be constructed with an unbounded period. The conventional generators of random numbers produce discrete sets of random variables. However, the mathematical analysis of stochastic processes requires smooth random variables, which have been developed in the current paper. Therefore, the presented results are of interest in various applications dealing with smooth stochastic functions.

Acknowledgements

The support of CAAM and the University of Mount Saint Vincent is gratefully

acknowledged. The author thanks a reviewer for helpful comments, which have improved the paper.

Conflicts of Interest

The author declares no conflicts of interest regarding the publication of this paper.

References

[1] Miroshnikov, V.A. (2023) Stochastic Chaos of Exponential Oscillons and Pulsons. *American Journal of Computational Mathematics*, **13**, 533-577. https://doi.org/10.4236/ajcm.2023.134030

[2] Miroshnikov, V.A. (2024) Wave Turbulence of Exponential Oscillons and Pulsons. *American Journal of Computational Mathematics*, **14**, 96-168. https://doi.org/10.4236/ajcm.2024.141004

[3] Miroshnikov, V.A. (2024) Theoretical Quantization of Exact Wave Turbulence in Exponential Oscillons and Pulsons. *American Journal of Computational Mathematics*, **14**, 203-239. https://doi.org/10.4236/ajcm.2024.142007

[4] Miroshnikov, V.A. (2023) Quantization of the Kinetic Energy of Deterministic Chaos. *American Journal of Computational Mathematics*, **13**, 1-81. https://doi.org/10.4236/ajcm.2023.131001

[5] Miroshnikov, V.A. (2023) Quantization and Turbulization of Deterministic Chaos of the Exponential Oscillons and Pulsons. BP International. https://stm.bookpi.org/QTDCEOP/issue/view/1045

[6] Miroshnikov, V.A. (2009) Spatiotemporal Cascades of Exposed and Hidden Perturbations of the Couette Flow. *Advances and Applications in Fluid Dynamics*, **6**, 141-165. http://www.pphmj.com/abstract/4402.htm

[7] Miroshnikov, V.A. (2012) Dual Perturbations of the Poiseuille-Hagen Flow in Invariant Elliptic Structures. *Advances and Applications in Fluid Dynamics*, **11**, 1-58. http://www.pphmj.com/abstract/6711.htm

[8] Abramowitz, M. and Stegun, I.A. (1965) Handbook of Mathematical Functions with Formulas, Graphs, and Mathematical Tables. 9th Edition, Dover Publications.

[9] Korn, G.A. and Korn, T.A. (2000) Mathematical Handbook for Scientists and Engineers: Definitions, Theorems, and Formulas for Reference and Review. Dover Publications.